NTNU – Trondheim
Norwegian University of
Science and Technology

Effect of ultrasound on the distribution of nanoparticles in tumor tissue

Kishia Stojcevska Søvik

Effect of ultrasound on the distribution of nanoparticles in tumor tissue

Kishia Stojčevska Søvik

June 28, 2013

Abstract

PC-3 prostate adenocarcinoma cells were injected subcutaneously in the hind leg of female Balb/c nude mice. After a few weeks of tumor growth, 200 μL of a solution containing gas bubbles stabilized by PBCA nanoparticles encapsulating nile red was intravenously administered. The mice were then divided into four treatment groups, three of which were treated with ultrasound, while the last group was not. The three different ultrasound treatments were (1) 1 MHz and MI = 0.1, (2) 1 MHz and MI = 0.4, and (3) 1 MHz and MI = 0.4 + 5 MHz and MI = 2.24. Blood vessels were stained using FITC-lectin. Freeze sections from the tumors were prepared and imaged in a confocal microscope. The images were quantitatively and qualitatively analyzed. No statistical difference was found between the different treatment groups from the quantitative analysis, as the standard deviations were too large. However, a qualitative difference could be observed between mice that were not treated with ultrasound and mice that were treated. It was concluded that the uptake in adipose tissue seemed to be improved after ultrasound.

Preface

This project report was written as part of the project "Multifunctional Nanoparticles in Cancer Diagnosis and Therapy" coordinated by Sabina Strand at the Department of Biotechnology, NTNU. The project is a collaboration between the Norwegian University of Science and Technology (NTNU), SINTEF and Trondheim University Hospital.

I would like to thank my supervisor Catharina de Lange Davies (Department of Physics) for being understanding and giving valuable feedback throughout the semester. Many thanks also go to my co-supervisor Siv Eggen (Department of Physics) for providing tumor sections, invaluable help and points of view, and to Astrid Bjørkøy (Department of Physics) for providing the Matlab routine and helpful advice. Finally, I would like to thank Ýrr Mørch (SINTEF) who made the nanoparticles for providing valuable information.

Contents

1 Introduction

Cancer is a devastating disease and a leading cause of death worldwide [38]. The major disadvantage related to conventional cancer therapy is that it is not specific. Conventional chemotherapeutics are toxic to all cells, thereby not only destroying cancerous cells, but also healthy tissue. In addition, chemotherapeutics can have quite serious side effects, e.g. heart damage with Doxorubicin. To limit the amount of side effects experienced by the patient, the dose given to the patient must be controlled. Limiting the dose comes at the expense of the amount of drug that reaches the actual pathological site, and hence the effect of the therapy.

Nanoparticles have the potential to aid in this respect. By using nanoparticles as drug carriers, the treatment can be made more tumor specific. Due to their large size, intravenously administered nanoparticles extravasate from the relatively large pores of blood vessels in tumors, and accumulate in the cancerous tissue. This is termed passive targeting. At the same time the nanoparticle carrier protects the healthy cells from the drug, meaning that the side effects are reduced. This again means that the chemotherapeutic dose can be increased and the therapy becomes more effective. By actively targeting the nanoparticles to certain cells by functionalizing them with ligands, the treatment can be made even more specific depending on tumor type.

Although the nanoparticles accumulate in the tumor interstitium, getting them to the cancerous cells is challenging as there are several factors hindering them. One of the largest obstacles is the high interstitial pressure of the tumor. Ultrasound can be used to help overcome the physical barriers for the nanomedicine and works by one or more of three mechanisms: hyperthermia, cavitation and radiation pressure. In combination with microbubbles, ultrasound has been shown to improve drug delivery.

In this report, confocal microscopy data from mice having received microbubbles made from a shell of PBCA nanoparticles encapsulating nile red, in combination with ultrasound therapy, is reviewed. The aim is to investigate how different ultrasound treatments affects the distribution of nanoparticles in tumor tissue.

2 Theory

2.1 Nanoparticles

Traditionally, nanoparticles are defined as particles with sizes up to 100 nm. In practice, however, particles larger than this are included in the definition. Nanoparticles possess some unique properties that their bulk equivalents do not, such as the small size, large surface area to volume ratio and high reactivity [51]. These properties may be utilized in medicine to overcome some of the limitations of traditional therapeutic and diagnostic agents [51]. Nanoparticles may have different shapes and may be constructed of different materials. They may be used for either diagnostic or therapeutic applications, or for theranostics, which is a combination of both of these [25].

2.1.1 Nanoparticles in Therapeutics

One major application for nanoparticles in therapeutics is as a drug carrier, protecting the drug from premature activation during transport to the diseased site [6]. The nanoparticle may be functionalized to bind specifically to certain cells, e.g. tumorous cells, increasing the dose arriving at the desired location and reducing the dose to healthy parts of the body. In cancer therapy, this reduces side effects of common chemotherapeutics, permitting use of even higher doses to increase the effectiveness of the therapy. A controlled release of the drug from the nanoparticle may be achieved by controlling the material composition of the nanoparticle and the way by which the drug is associated with the carrier [6]. Some of the most common types of nanoparticles for medical applications are described next and shown in Figure 1.
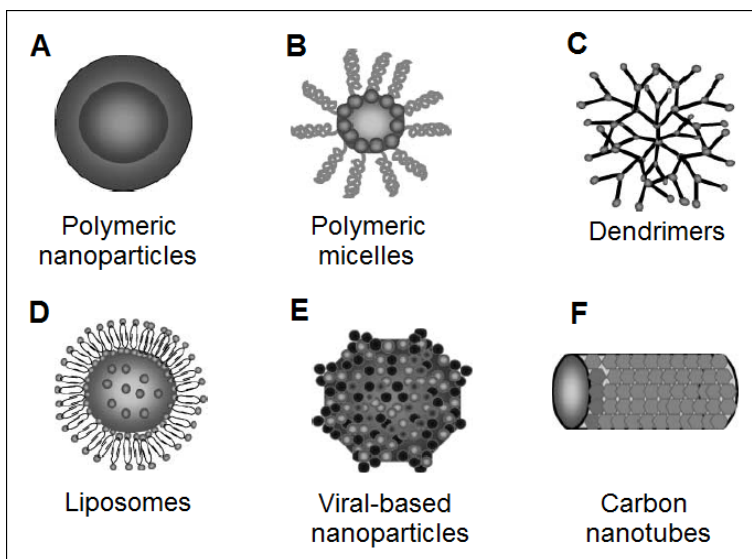
Figure 1: Different types of nanoparticles [10].

Polymeric Nanoparticles   The drug can be either physically entrapped or co-valently bound to a polymer matrix, depending on the method of preparation [10]. Polymeric nanoparticles (Figure 1A) usually have the structure of capsules or spheres [17] and can be made from naturally occurring polymers such as albumin, chitosan and heparin [10] or from synthetic polymers such as polyethylene glycol (PEG), poly-L-glutamic acid (PGA) or poly(butyl cyano acrylate) (PBCA).

Polymeric Micelles   Polymeric micelles (Figure 1B) are spherical or globular core/shell structures formed by (self-)assembly of amphiphilic block copolymers in aqueous media [10, 17]. The micelle usually has a hydrophilic shell region which stabilizes a hydrophobic core region that serves as a reservoir for hydrophobic drugs [10]. Hydrophilic drugs can be loaded if the interior of the micelle is hy-drophilic. The drug can be loaded either by physical encapsulation or by chemical covalent attachment, as for polymeric nanoparticles [10].

Dendrimers   Dendrimers (Figure 1C) are three-dimensional branched polymeric structures, composed of multiple highly branched monomers that emerge radially from a multifunctional central core molecule [10, 17]. Some properties that make them attractive for drug delivery are their monodispersity and water solubility, and the interior dendritic channels where drugs may be loaded [10, 17]. Drug

molecules may also be attached to the dendrimer surface [17]. Dendrimers can host both hydrophobic and hydrophilic molecules [17].

Liposomes Liposomes (Figure 1D) are self-assembling closed spherical structures composed of lipid bilayers surrounding a central aqueous space [10]. They are classified as either unilamellar or multilamellar according to the number of lipid bilayers [17]. Unilamellar liposomes entrap hydrophilic drugs, whereas multilamellar liposomes can load hydrophobic drugs [17].

Viral-based Nanoparticles Viral-based nanoparticles (Figure 1E) are well-characterized, monodisperse and highly symmetrical structures [50]. They are based on the structures of naturally occurring viruses. The internal cavity of the structure can be filled with e.g. drugs or other nanoparticles, and the external surface can, as for the other classes of nanoparticles, be functionalized for targeting purposes [50]. Besides this artificial targeting, some viruses have a natural affinity for certain receptors that are often up-regulated on tumor cells [10].

Carbon Nanotubes Carbon nanotubes (Figure 1F) are ellipsoid carbon tubes composed of benzene rings [10, 17]. There are some health concerns and toxicity problems related to carbon nanotubes due to their complete insolubility in all solvents [10]. However, the surface can be chemically modified to render them water soluble, and they may be functionalized so that they can be linked to active molecules [10] such as drugs or targeting ligands. Atoms may also be trapped in the interior of the tubes [17].

2.1.2 Nanoparticle Characeristics Affecting Drug Delivery

The main motivation for loading drugs in nanoparticles, besides protecting them from premature activation, is to passively target the drugs to tumor tissue by utilizing the enhanced permeability and retention (EPR) effect (see Section 2.2.5). In order to do this, the nanoparticles must remain in the blood stream for a considerable time without being eliminated by the reticuloendothelial system (RES) [10]. The mean half-life of conventional nanoparticles with a non-modified surface after intravenous administration is 3-5 minutes [6]. One of the advantages of using nanoparticles as drug carriers is that the size of the particle and the surface characteristics can be adjusted to considerably increase the circulation time of the drug in the body [10].

Size   Nanoparticles used in drug delivery systems should have a size large enough to prevent rapid leakage into blood capillaries, but small enough to escape capture by fixed macrophages in the RES [10]. To increase the circulation time in the body, the size of the nanoparticle must be above the renal clearance threshold [30]. The renal clearance is inversely proportional to the size of the particle, and hence circulation time increases as the size of the particle increases [24].

Surface Characteristics and PEGylation   Clearance of nanoparticles from the body by the RES depends not only on the size of the particles, but also on the surface characteristics [24]. To escape macrophage capture nanoparticles should ideally have a hydrophilic surface [10]. This can be achieved either by using polymeric micelles with a hydrophilic shell as a nanocarrier, or by coating the surface of other nanoparticles with a hydrophilic copolymer [10]. The most common approach is to coat the nanoparticle surface with the hydrophilic polymer PEG, typically referred to as PEGylation [24].

2.1.3   Nanoparticles in Diagnostics

The contrast of images obtained using common diagnostic imaging modalities, such as MRI, X-ray and ultrasound, can be enhanced by using contrast agents while imaging. Many of the advantages of using nanoparticles for therapeutic purposes are also advantages of using nanoparticles as contrast enhancers. When using nanoparticles as contrast agents, longer imaging duration is possible due to the long circulation time of nanoparticles in the body [16]. In addition, the nanoparticles may be targeted, e.g. to specific organs, for more specific imaging [3].

Ultrasound is a non-invasive, low-cost diagnostic imaging tool. Nanoparticle contrast enhancers enable ultrasonic imaging in situations where it was previously impossible due to poor contrast. Microbubbles are a type of particles that are currently used as contrast agents for ultrasonic imaging. Reflection of sound is increased by creation of an acoustic impedance mismatch between fluids and tissues [49]. Microbubbles do however also have potential applications in therapeutics [49], and an advantage of using microbubbles in medicine is that the same particle can be used both for therapy and diagnostics. The topics of ultrasound and microbubbles are further reviewed in Section 2.5.

2.2   Cancer Tissue

In healthy tissue there is a balance between cell division and cell differentiation, ensuring that the number of dividing cells does not increase [2]. A disruption of

this balance results in an accumulation of dividing cells and a mass of growing tissue termed a tumor. Tumor growth is quick if the cells are dividing rapidly and slower if the cells are dividing more slowly, but since cells are produced in greater numbers than needed, the tumor will continue to grow regardless of the speed of cell division [2]. Tumors are classified as benign if they grow in a confined local area, and malignant if they can invade surrounding tissues, enter the bloodstream and spread to distant locations [2]. Malignant tumors are termed cancer, and the ability of cancer to grow in an uncontrolled manner and spread to distant parts of the body makes it a potentially life-threatening disease [2].

2.2.1 Angiogenesis

Mammalian cells are located within 100 to 200 μm of blood vessels, which is the diffusion limit for oxygen, to assure that they receive the oxygen and nutrients required for their survival [7]. Hence, for tumors to be able to grow beyond a few millimeters in diameter, angiogenesis, that is, the growth of new blood vessels, is required [2]. To trigger angiogenesis, tumors increase the production of angiogenesis activators such as vascular endothelial growth factor (VEGF) and fibroblast growth factor (FGF), and simultaneously decrease the production of angiogenesis inhibitors [2].

2.2.2 Metastasis

The cancer cells are able to spread throughout the body, or metastasize, once angiogenesis has been triggered at the tumor site [2]. Following angiogenesis, three other steps are also neccessary in order for metastasis to occur [2]. The first step involves cancer cells gaining access to the blood stream by invading surrounding tissues and penetrating the walls of lymphatic and blood vessels. Once they have accessed the blood stream, the cancer cells are transported by the circulatory system throughout the body. Lastly, the cancer cells leave the blood stream and establish new metastatic tumors in particular organs [2]. Metastasis can not occur if one of these steps is prevented [2].

2.2.3 Tumor Vasculature

The movement of compounds through the vasculature is affected by vascular morphology [24]. Blood vessels in tumors differ greatly from those in normal tissues, both on a macroscopic and on a microscopic level.

On the macroscopic level, tumor vessels lack hierarchic branching from larger vessels into successively smaller vessels that feed a capillary bed [24] (Figure 2). They are heterogeneously distributed in the tumor tissue, dilated and tortuous, and some spaces are even left avascular [24]. Microscopically, the vessel wall structure is abnormal and irregular. Compared to vessel walls in normal tissues, interendothelial junctions are wider, the thickness of the basement membrane is abnormal, pores are considerably larger and there are large numbers of fenestrae and transendothelial channels [24]. The irregularity of the vessel walls render them leaky and hyperpermeable in some places, while not in others [24].
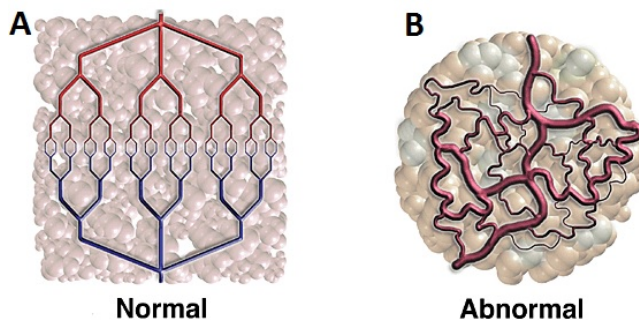

Figure 2: Differences between blood vessels in normal (A) and cancerous (B) tissue. Tumor blood vessels are heterogeneous, dilated and tortuous, and lack hierarchic branching. Source: [22].

The large number of proliferating cells in the tumor also adds to the irregularity and spatial heterogeneity of the vessels by compressing them, sometimes to such an extent that the vessels collapse [24]. As a result, some regions can be left unperfused. This may lead to hypoxia and acidosis, causing resistance to several cytotoxic drugs and compromising the cytotoxic functions of immune cells [24].

2.2.4 Lymphatic Network

Proliferating tumor cells compress not only blood vessels, but also lymphatic vessels [24, 40]. The interstitial fluid balance is normally maintained by the lymphatic network, which drains excess fluid from healthy tissue. When lymphatic vessels in the tumor tissue collapse as a result of the compression, the fluid drainage becomes inefficient [24]. This tends to happen especially in the center of the tumor, leaving functional lymphatic vessels only in the tumor periphery [24]. Coupled with the fluid leakage from tumor blood vessels, this inefficient fluid drainage contributes to interstital hypertension [24].

2.2.5 Enhanced Permeability and Retention Effect

The EPR effect is a phenomenon that results in a preferential accumulation of macromolecules in tumor tissue over normal tissue. The leakiness of the tumor blood vessels means that blood plasma components end up in the tumor interstitium, and the poor lymphatic clearance means that macromolecules are not removed from the tissue [20]. As the extravasation from tumor blood vessels continues, macromolecules accumulate.
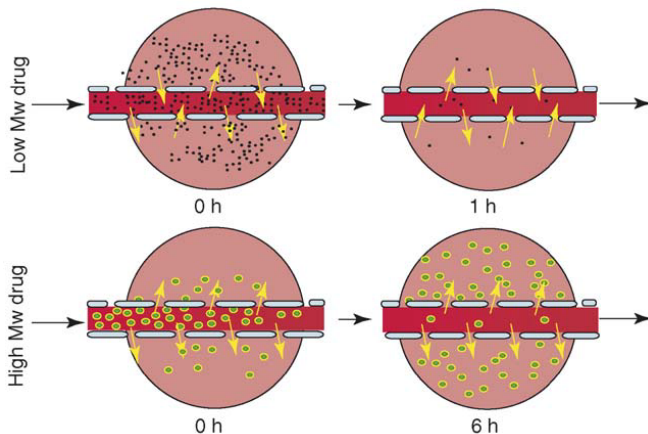

Figure 3: Low molecular weight (Mw) drugs are able to diffuse freely across the tumor vessel walls, owing to their small size. As the blood plasma drug concentration is reduced over time, the effective concentration of drug in the tumor is also diminished. However, the large size of high Mw drugs means that they are not able to diffuse back into the blood stream, and hence macromolecular drugs accumulate in the tumor tissue over time. Source: [20].

Low-molecular-weight drugs, such as antibiotics and many chemotherapeutic agents, reach both normal and tumor tissues by free diffusion-dependent equilibrium [30], and are returned to the circulating blood by diffusion [29] and cleared by the renal system [20]. Hence, the EPR effect does not apply, and they do not accumulate, even in tumor tissue. This is the background for using macromolecular drugs, e.g. loading conventional chemotherapeutics into nanoparticle carriers, instead of the low-molecular-weight drugs that are normally used to treat cancer today. Since the EPR effect does apply for macromolecules, it can be utilized to selectively target macromolecular drugs to solid tumors [33]. This is becoming a gold standard for the design of new anticancer agents [33].

2.3 Barriers for Drug Delivery

Once a drug has been administered, it needs to be transported from the site of injection to the part of the body where it's supposed to excert its effect. Drug delivery to the intended site is dependent on three transport steps. These are vascular transport, transport via blood vessels; transvascular transport, transport across the vessel wall; and interstitial transport, transport through the tumor tissue toward the target cells [9] (see Figure 4). In normal tissues, these transport steps are highly efficient, as they developed for effective oxygen and nutrient transport [9]. However, the abnormal physiology of tumor tissue, described in Section 2.2, gives rise to transport barriers that limit drug delivery to tumors [9].
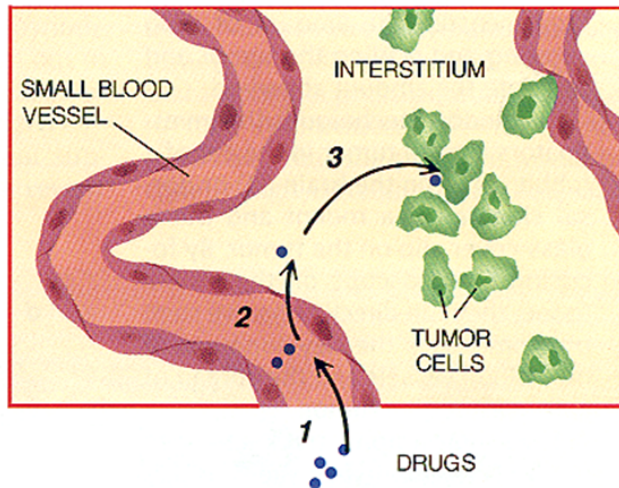

Figure 4: Drugs must travel through the blood stream (vascular transport), across the vessel wall (transvascular transport) and through the interstitium (interstitial transport) to reach the tumor cells. Source: [21].

2.3.1 Abnormalities Contributing to Transport Barriers

There are four major abnormalities of tumor tissue that limit drug delivery [9]. Each of these can limit multiple transport processes [9]. The first three abnormalities have previously been described in Section 2.2.

Accumulated Solid Stress The large number of proliferating cells, together with an overproduction of interstitial matrix molecules, in tumor tissue leads to

an accumulation of solid stress. This is the first abnormality of tumor tissue that limits drug delivery. The solid stress compresses blood vessels, which leads to reduced perfusion to many regions of the tumor [9]. The poor perfusion means that drug distribution is limited [9].

Immature Tumor Vasculature   Secondly, the immaturity of the tumor vasculature also limits drug delivery. The high tortuosity of tumor blood vessels leads to an increased geometric resistance, which slows blood flow [9]. In addition, the hyperpermeability of the blood vessels means that the viscosity of the blood increases due to fluid loss, which further slows blood flow [9]. This combination of effects means that blood flow through tumor tissue is very slow and heterogeneous compared to normal tissue, and is a major barrier to vascular transport and hence drug delivery [9].

Elevated Interstitial Fluid Pressure   Thirdly, the compression of lymphatic vessels combined with the leakiness of the blood vessels means that fluid accumulates in the interstitial compartment of the tumor. This accumulation of fluid leads to an elevated interstitial fluid pressure (IFP) inside the tumor. The IFP becomes almost equal to the microvascular pressure [4], resulting in a lack of interstitial fluid pressure gradient, and hence the driving force for convective interstitial transport is diminished [9]. Diffusion is left as the main transport mechanism for drugs in the bulk of the tumor, resulting in short penetration distances and poor drug distribution [9].

Dense Interstitial Structure   The last abnormality of some types of tumor tissue that reduces drug delivery is the dense interstital structure of the tumor [9]. The extracellular matrix (ECM) of animal cells consists of three classes of molecules [2]. The first class is structural proteins, and the most important of these are collagens, accounting for much of the strength of the ECM, and elastins, providing the elasticity and flexibility [2]. The structural proteins are embedded in a matrix consisting of proteoglycans, which is the second group of molecules in the ECM [2]. Proteoglycans are glycoproteins in which a large number of glycosaminoglycans, a type of large carbohydrates, are attached to a single protein molecule [2]. The last group of ECM molecules are the adhesive glycoproteins, of which the two most common are fibronectins and laminins [2]. Adhesive glycoproteins bind proteoglycans and collagen molecules to each other and to receptors on the membrane surface [2].

The high cellularity of tumors and the overproduction of interstitial matrix molecules can cause the matrix to be compressed into a tortuous and dense network [9], depending on tumor type. Some tumor types contain a lot of enzymes that break

down the ECM, creating a large interstitial space [23]. For tumors with a dense interstitium, the interstitial density generally increases toward the tumor center [31]. Diffusion is slow as the matrix is dense, and diffusion path lengths from blood vessels to target cells are extremely long due to the tortuosity of the matrix [9]. This greatly limits drug delivery. As many drugs bind to matrix and cellular components, interstitial transport rates become even lower, further limiting drug delivery [9].

2.3.2 Diffusion as the Main Transport Mechanism

Both transvascular and interstitial transport normally occur through a combination of diffusion and convection [9] (see Figure 5). Diffusion is a much slower process than convection, particularly for large particles [24].
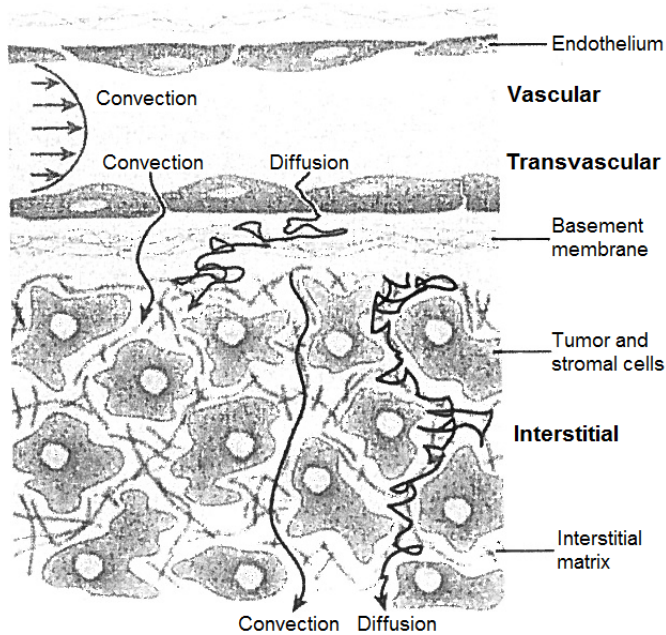

Figure 5: Transport steps. Both transvascular and interstitial transport normally occur through a combination of diffusion and convection. Diffusion is a much slower process than convection. Source: [9].

As mentioned in Section 2.3.1, a direct consequence of the lack of IFP gradient in tumors is that diffusion is left as the main transport mechanism [24], both for transvascular and interstitial transport. The reduced transvascular transport lim-

its drug delivery to tumor tissue. It is even possible for the IFP to exceed the microvascular fluid pressure and hence cause intravasation of material back into the blood supply [24]. For interstitial transport, the diffusion rate in the interstitial matrix depends on the size and charge of the particle, as well as psysicochemical properties of the matrix [24]. Diffusion of small-molecular drugs such as chemotherapeutics is fairly rapid, but the diffusion of comparably large nanoparticles is considerably hindered by interactions with the interstitial matrix [24]. In addition, electrostatic forces develop between charged particles and charged components of the interstitial matrix [24]. This can further hinder diffusion.

2.3.3 Non-uniform Delivery

As the pores in tumor blood vessels are larger than in normal blood vessels, drug-loaded nanoparticles are able to extravasate into the tumor interstitium [24]. However, the heterogeneous distribution of pore sizes means that the extravasation and delivery of drugs is non-uniform [24].

Once the particles have reached the interstitium, uniform distribution in tumor tissue is hindered by the heterogeneous distribution of interstitial matrix components [24]. The matrix can be separated into a viscous, high-collagen phase and an aqueous, low-collagen phase [24]. The viscous phase greatly hinders particle movement, while the diffusivity in the aqueous phase is similar to that in water [24]. Hence, the heterogeneous distribution of phases leads to non-uniform distribution in the tumor.

2.4 Uptake Mechanisms in Cells

In order to exert its effect, a drug that has an intracellular target must be internalized into the cells once it has reached its site. There are several mechanisms by which material can reach the interior of the cell.

2.4.1 Simple Diffusion

Simple diffusion, the unassisted net movement of a solute along its concentration gradient, is the most straightforward way for a solute to cross the cell membrane [2]. It is a relevant means of transport only for some small, relatively non-polar molecules such as oxygen, carbon dioxide, water and ethanol, owing to the hydrophobic interior of cell membranes [2]. The movement of water across a selectively permeable membrane from regions of lower solute concentration to regions

of higher solute concentration is termed osmosis [2]. Diffusion is always movement toward equilibrium, and hence a spontaneous process [2]. There are three main factors affecting diffusion of solutes: size, polarity and charge.

Size   Lipid bilayers are generally more permeable to molecules the smaller they are [2]. Water, oxygen and carbon dioxide are the smallest molecules relevant to cell function, but even molecules as small as these can not diffuse freely across the membrane; for example, compared to free diffusion in the absence of a membrane, water molecules diffuse 10 000 times slower across a bilayer [2]. Molecules with molecular weights (Mw) of above about 100 Da, such as glucose (Mw 180 Da), are unable to cross the cell membrane by simple diffusion [2]).

Polarity   Since nonpolar, or hydrophobic, molecules dissolve more readily in the hydrophobic phase of the lipid bilayer than do polar molecules, the cell membrane is more permeable to nonpolar molecules compared to polar molecules of similar size [2]).

Charge   Polar molecules in general, and ions in particular, have a strong association with water molecules, forming a shell of hydration [2]. The water molecules must be removed in order for such solutes to move into the membrane [2]. As an input of energy is required to strip off the water molecules, the formation of shells of hydration hinders ion transport across membranes [2].

2.4.2   Facilitated Diffusion and Active Transport

Although a few types of molecules are able to cross the membrane at reasonable rates by simple diffusion, most are dependent on an alternative means of transport as they are either too large or too polar [2]. Transport proteins in the cell membrane mediate the movement of such molecules across the membrane [2]. Most of them are highly specific [2]. If the solute moves along its gradient, the process requires no input of energy and is termed facilitated diffusion [2]. If, however, the solute needs to be moved against its gradient, additional energy is required. This process is called active transport. Transport proteins involved in active transport couple an energy demanding process (the movement of a solute against its gradient) to an energy-yielding one (usually ATP hydrolysis) [2].

2.4.3 Endocytosis

Material that can not cross the plasma membrane by either of the transport mechanisms specified above, may be internalized by a process termed endocytosis. Once endocytosed, the material is separated from the cytosol by a portion of the plasma membrane, and hence is not really "inside" the cell.

During endocytosis, the plasma membrane invaginates and then pinches off to form an endocytic vesicle [2] (Figure 6). Early endosomes are formed as endocytic vesicles coalesce with vesicles from the trans-Golgi network containing lysosomal enzymes [2]. The early endosome matures over time to form a late endosome. During this process the pH of the lumen drops and the organelle can no longer fuse with endocytic vesicles [2]. In a final step the pH of the lumen is further lowered to activate acid hydrolases. This is accomplished in one of two ways. The late endosome is either transformed into a lysosome when ATP-dependent proton pumps lower the pH of the lumen, or the late endosome fuses with an already existing lysosome and transfers its content to its acidic lumen [2]. The material ingested during endocytosis is digested in lysosomes.
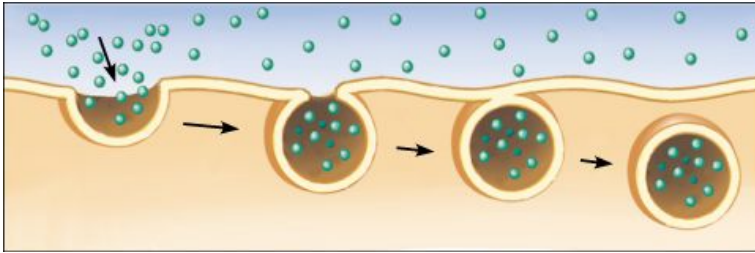

Figure 6: Endocytosis. The plasma membrane invaginates and then pinches off to form an endocytic vesicle. Source: [34].

Receptor-Mediated Endocytosis   Receptor-mediated endocytosis is a specific internalization mechanism where receptors found on the plasma membrane are used to aquire material from the outside of the cell [2]. It is dependent on the protein clathrin and is hence also referred to as clathrin-dependent endocytosis. If nanoparticles are functionalized with the right ligands, receptor-mediated endocytosis may be the mechanism of their internalization.

The process begins with the binding of specific molecules called ligands to their receptors on the cell surface. Receptor-ligand complexes then diffuse in the plasma membrane and accumulate in special membrane regions called coated pits [2]. The receptor-ligand complex accumulation triggers accumulation of additional proteins, among them clathrin, that are required for membrane curvature and invagina-

tion [2]. The membrane continues to invaginate until the pit pinches off, forming a coated vesicle, at which point the clathrin coat is released, leaving an uncoated vesicle [2]. The uncoated vesicle is then free to fuse with an early endosome.

Clathrin-Independent Endocytosis   Apart from the clathrin-dependent type of endocytosis, there are also other types of endocytosis that are not dependent on clathrin. Of these clathrin-independent pathways, caveolin-dependent endocytosis and macropinocytosis are the most important.

Caveolin-dependent endocytosis is endocytosis via caveolae, which are flask-shaped invaginations found in the plasma membrane of many cell types [41]. Caveolins are essential for the formation and stability of caveolae [41]. When material is taken up by this pathway, the caveolae pinch off and become caveolin-coated endocytic vesicles [41]. Once internalized, caveolar vesicles enter sorting compartments called caveosomes, which are distinct from endosomes, and are then distributed mainly to the ER and Golgi complex [41].

Macropinocytosis is a form of endocytosis where single surface lamellipodia bend, giving rise to curved ruffles, and seal back onto the plasma membrane, forming macropinosomes [13]. In this way the cell internalizes large volumes of extracellular fluid, as well as solid material present in the extracellular fluid [13].

2.5   Overcoming the Barriers

To enhance drug delivery, the barriers of drug delivery must be overcome. This is normally done by some physical means. One way is to use ultrasound. Pressure waves produced by ultrasound can be concentrated through cavitating gas bodies, such as microbubbles (see Section 2.5.2), to produce forces that permeabilise cell membranes and disrupt the drug carrying vesicles [42]. In this way they assist in overcoming the barriers for drug delivery, and the presence of microbubbles enhances ultrasonic delivery [42].

2.5.1   Ultrasound

Ultrasound is the transmission of pressure waves at frequencies above what the human ear can detect. Ultrasonic waves are the actual movement of molecules in the medium as the pressure changes; the medium is compressed at high pressure and expanded at low pressure, and hence ultrasound can act physically on biomolecules and cells [42]. The waves are absorbed relatively little by water, flesh

and other tissues, and this safe, non-invasive and painless technique can be used to transmit energy into the body at precise locations [42].

Ultrasonic treatment can be used to enhance drug delivery by several mechanisms. The simplest of these is the oscillation of the insonated fluid, which increases the effective diffusivity of molecules [42]. The transport of any drug will be augmented by the oscillatory motion of the fluid. Other than this, there are three main effects of ultrasound that are taken advantage of to enhance drug delivery. They are thermic effects, cavitation and radiation force.

Thermic Effects   Ultrasound can be used to induce hyperthermia by focusing the beam down to a small size on the targeted tissue. Acoustic energy is removed from the ultrasound wave and absorbed by the tissue [19]. The power/area becomes very large and the tissue absorbs thermal energy, resulting in heating of the tissue [42]. Hyperthermia can be used either for direct treatment of small and localized tumors by high-intensity ultrasound [8, 35], or to enhance radiation therapy and chemotherapy by low-intensity ultrasound [35, 18]. In drug delivery, hyperthermia works by heating the drugs, drug carriers and/or the tissues receiving the drugs [42].

Cavitation   The term cavitation refers to the creation, oscillation, growth and collapse of gas bubbles within a medium exposed to an ultrasonic field [19, 1]. The acoustic pressure within an ultrasonic field acts on gas bubbles to make the bubble radius vary [19]. The bubble expands at low pressure and contracts at high pressure [42], behaving as an oscillator with a natural resonant frequency [19]).

If the oscillation is stable, it is referred to as "stable" cavitation (Figure 7A). During stable cavitation, a circulating fluid flow called microstreaming is created around the bubble [37]. In addition, a phenomenon called acoustic pressure results in bodies more dense than the suspending fluid being pushed toward the bubble [36]. Most drug carriers containing drugs will be convected toward the bubble and into the microstreaming field, since they are usually more dense than water [42]. The velocities and shear rates of the microstreaming eddies are proportional to the amplitude of oscillation, and near the bubble surface they are high enough to cause stress to cells and vesicles [42]. At high amplitudes, the associated shear forces are capable of inducing hemolysis [45] and disrupting drug carriers such as liposomes [32], enhancing dispersive drug transport [42].

As the ultrasonic intensity increases, the amplitude of gas bubble oscillation also increases. At some point, the fluid wall moving inward has sufficient inertia that it does not reverse direction when the acoustic pressure reverses. Instead, it continues to compress the gas in the bubble to a very small volume, creating extremely

high pressures and temperatures [5], and the bubble collapses. This type of cavitation is called collapse cavitation. The collapse produces very high shear stresses in the collapse region, a shock wave (Figure 7B), and free radicals resulting from the high temperatures, all three of which can be detrimental to cells or vesicles [42]. The collapsed bubble often fragments into smaller bubbles serving as cavitation nuclei, which grow in size and eventually collapse again [5]. If the collapse is near a solid surface, a liquid jet is ejected toward the surface at sonic speed [5], capable of piercing e.g. blood vessel walls, skin, large cells or semi-rigid vesicles [42] (Figure 7C).
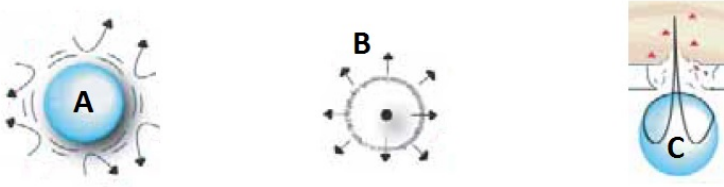
Figure 7: Stable cavitation of a gas bubble (A), collapse cavitation emitting a shock wave (B), and collapse cavitation near a surface, with ejection of liquid jet (C). Source: [42].

The occurrence of collapse cavitation for a particular spherical bubble nucleus in a given liquid depends on the acoustic pressure amplitude, the acoustic frequency and the bubble radius [19]. An expression called the mechanical index (MI) can be considered to be an indicator of the likelihood of collapse cavitation [19]. It is defined as

$$\text{MI} = \frac{p_\text{r}}{\sqrt{f}},$$
(1)

where p_r is the peak rarefactional pressure in MPa and f is the frequency in MHz [19]. If the threshold MI of 0.7 is not reached, the probability of collapse cavitation is considered negligible [19]. The maximum allowed MI value that is allowed for diagnostic machines in the US is 1.9 [19].

Radiation Pressure   Radiation pressure is a secondary physical effect that can be generated by an ultrasonic field [19]. For a continuous acoustic wave it is a steady, small force that acts in the direction of propagation of the wave [19]. Radiation pressure leads to a force on particles in the ultrasonic field, which can result in particle movement for small particles [19].

2.5.2   Microbubble-Enhanced Ultrasound

Microbubbles used for ultrasound contrast enhancement are usually 1-4 μm in diameter, and are hence restricted to the vascular compartment [26]. They can be gas bubbles stabilized by surfactants, gas bubbles with a shell made from phospholipids, proteins or polymers [26], or they can even be made from a shell of nanoparticles.

The effect of using microbubbles combined with ultrasound in drug delivery has previously been proven by others. For example, Kinoshita et al. [27] were able to deliver Herceptin to the central nervous system of mice by using microbubbles combined with ultrasound to open the blood-brain barrier. Lawrie et al. [28] reported that ultrasound exposure in the presence of microbubble contrast agents enhanced transgene expression *in vitro* approximately 300-fold after naked DNA transfections, compared to naked plasmid DNA alone. Rapoport et al. [44] showed that administration of microbubble-encapsulated Doxorubicin combined with ultrasound treatment reduced tumor growth in mice. Escoffre et al. [12] observed a decrease in tumor growth and perfusion and an increase in tumor necrosis in nude mice treated with Irinotecan with microbubble-assisted ultrasound. Todorova et al. [48] reported significant tumor growth inhibition relative to control tumors for ultrasound-stimulated microbubble (USMB) treatment only, and an even stronger growth inhibition for USMB in combination with metronomic Cyclophosphamide.

2.6   Confocal Laser Scanning Microscopy

In biomedical sciences, confocal laser scanning microscopy (CLSM) is used for imaging fluorescently labeled tissues, either fixed or living [39]. The main advantage of confocal imaging lies in the ability of the microscope to eliminate fluorescence from areas of the specimen that are outside a focal plane. The spatial filtering characteristic of the confocal approach is achieved by placing a variable pinhole aperture in the image plane, in front of the detector [46] (7 in Figure 8). The pinhole assures that only light emanating from the focal plane is passed through to the detector [46]. CLSM offers a slight increase in resolution compared to a conventional wide-field light microscope, and it has bridged the gap between the commonly used techniques light microscopy and transmission electron microscopy [39]. CLSM produces an optical section of the specimen, and is hence a non-invasive method using light rather than physical means to section the specimen [39]. Thus, the confocal method allows for imaging of living specimens [39].
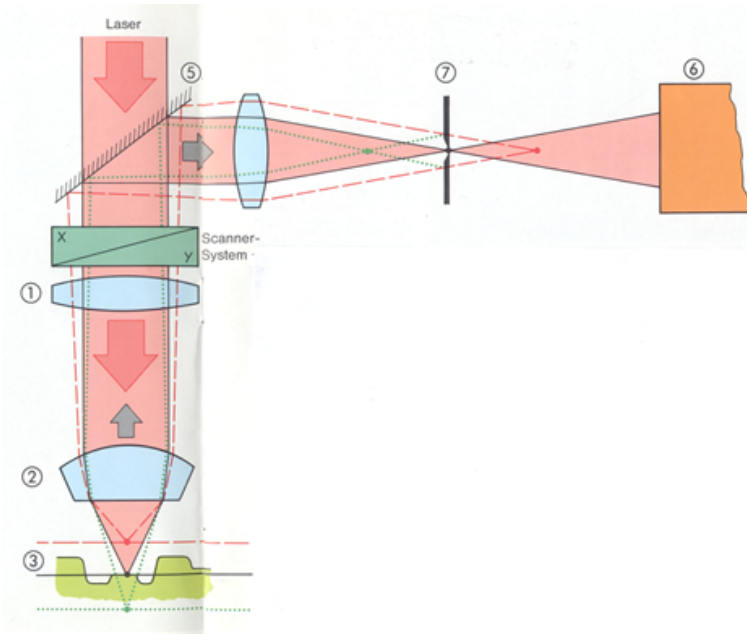
Figure 8: Confocal Laser Scanning Microscope. Source: Zeiss.

The illumination of the specimen in a CLSM is achieved by scanning a laser beam across the specimen in a raster pattern. The laser beam is focused to a spot by an objective lens, and scanning mirrors are used to control the position of the laser spot [2]. As the laser beam is scanned across the specimen, fluorescent light is emitted from fluorophores in the specimen. The fluorescence is red shifted compared to the laser as the wavelength is slightly longer. The emitted fluorescence is collected by the objective lens and returned along the path of the original incoming light [2]. A dichroic mirror is used to separate the incoming light from the fluorescence, as it transmits light with the wavelength of the fluorescence and reflects light with the wavelength of the laser beam [2]. The transmitted fluorescence then passes through the pinhole aperture, and light from the focal plane reaches the detector.

2.6.1   Spectral Imaging and Linear Unmixing

If the specimen is subject to artefacts arising from autofluorescence, spectral imaging combined with linear unmixing can be used to separate mixed fluorescent signals [11].

Spectral imaging merges spectroscopy and imaging to provide a complete spectrum

of the specimen at every pixel location [11]. Hence, a spectral image stack, often referred to as a lambda stack, can be considered as either a collection of images, each measured at a specific wavelength, or as a collection of different wavelengths at each pixel location [11].

Lambda stacks are virtually impossible to analyze by visual inspection, and require dedicated software for interpretation and presentation of the results [11]. Regardless of the spectral overlap with other probes, each probe has a unique spectral signature, or an emission fingerprint, that can be determined by linear unmixing of lambda stacks [11]. The result is conversion of a lambda stack into individual images representing the signal profile for each fluorescent probe [11].

Spectral imaging and linear unmixing can be used to reduce or completely eliminate unwanted autofluorescence from images [11]. This is accomplished by treating the autofluorescence as a separate fluorophore with a distinct emission fingerprint [11].

3 Materials and Methods

3.1 Experimental

3.1.1 Gas Bubbles and Nanoparticles

The gas bubbles that were administered to the mice are made from a shell of the poly(butyl cyano acrylate) (PBCA) nanoparticles YM-59. The bubbles are made with 1 % bovine serum albumin for stabilization. The size of the bubbles is 1-6 μm.

YM-59 are PBCA nanoparticles with encapsulated nile red and 1,1'-dioctadecyl-3,3,3',3'-tetramethylindotricarbocyanine iodine (DiR), sodium dodecyl sulfate (SDS) as surfactant and Jeffamin M-1000 as PEG. The polymer is crossbound. The size is 194 nm and the polydispersity index is 0.07. The particles have a low PEG density.

Both the YM-59 nanoparticles and the gas bubbles stabilized by the nanoparticles were made by SINTEF.

3.1.2 Ultrasound Exposure

PC-3 prostate adenocarcinoma cells (American Type Culture Collection, Manassas, VA, USA) were injected subcutaneously in the hind leg of female Balb/c nude mice (C.Cg/AnNTac-$Foxn1^{nu}$ NE9, Taconic, Lille Skensved, Denmark) as a 50 μL suspension containing 3×10^6 cells. After 3-6 weeks of tumor growth, when the tumor diameter had reached between 5 and 10 mm, 200 μL of a solution containing gas bubbles stabilized by YM-59 was administered intravenously. Following administration, the mice were divided into four treatment groups, three of which received different ultrasound treatments that are presented in Table 1. Ultrasound treatment begun about 30 seconds after administration. The last group was a negative control and received only nanoparticle stabilized gas bubbles, but no ultrasound treatment. In addition, one mouse did not receive ultrasound or gas bubbles. 100 μL fluorescein-labeled *Lycopersicon esculentum* (Tomato) lectin (FITC-lectin) (Vector Laboratories) diluted to 1 mg/mL with 0,9 % NaCl was injected intravenously to label blood vessels. FITC-lectin was allowed to circulate for 5 minutes before the mice were euthanized. The tumor was then excised and embedded in OTC Tissue Tec (Sakura, Alphen aan den Rijn, The Netherlands) and frozen in liquid N_2.

Table 1: The four different ultrasound treatments that the mice were exposed to. f is the frequency of the ultrasound and p_r is the acoustic pressure. Mechanical index MI was calculated from (1).

	f	p_r	MI	Pulse duration	PRF	Insonation time
US 1	1 MHz	-0.1 MPa	0.1	10 cycles	3000	2 min
US 2	1 MHz	-0.4 MPa	0.4	10 cycles	3000	2 min
US 3	1 MHz	-0.4 MPa	0.4	10 cycles	3000	2 min
and	5 MHz	-1.6 MPa	2.24	20 cycles	1000	10 in each spot

The difference between US 1 and US 2 was the MI. The purpose of US 1 was to make the bubbles oscillate without collapsing, while the purpose of US 2 was to induce bubble collapse to free the nanoparticles, which hopefully then would cross the vessel wall. The purpose of US 3 was to see if an effect of radiation pressure could be observed. The first part of the ultrasound treatment in US 3 was the same as for US 2, hence the goal was to get the nanoparticles across the vessel wall. The second part of US 3 generated a positive pressure of 7.1 MPa, and was designed to increase the probability of achieving a radiation force to push the nanoparticles further into the tumor tissue.

3.1.3   Tumor Sections

The procedure for sectioning of the tumor is shown in Figure 9. The top 500 μm of the tumor was removed to make sure the sections were from inside the tumor. 25 frozen sections were then made from each tumor. Every section has a thickness of 25 μm. Five sections were made from five different positions in the tumor, with 250 μm between each position, meaning that sections 1-5 are from the most superficial position, section 6-10 from the next position, etc. One section out of the five from each position was randomly chosen and imaged, five sections in total from each tumor. The sections were mounted to objective glass slides and stored in a freezer at -88°C.
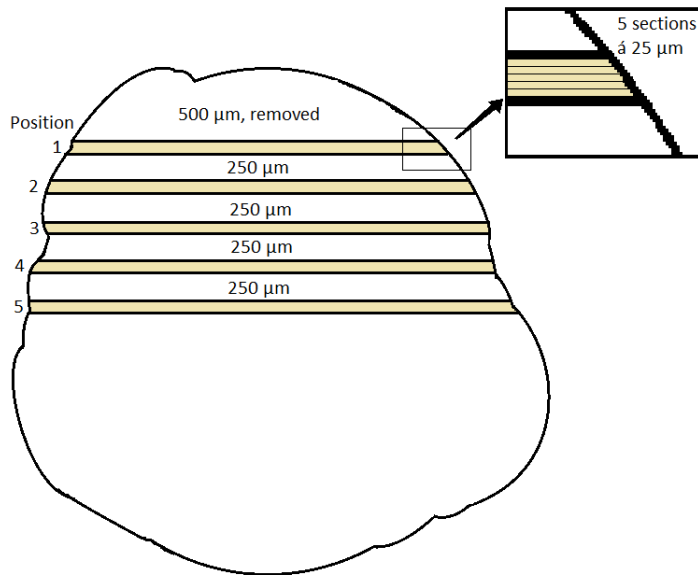
Figure 9: Average total fluorescence for one section, averaged over each treatment group. How the sections are made.

3.1.4 Section Preparation

For microscopic examination, the sections were removed from the freezer and 40 μL of Vectashield mounting medium (Vector Laboratories, Burlingame, CA, USA) was carefully applied on top of the tumor sections on the glass slides, making sure no air bubbles were introduced. A cover glass was then placed on top of the objective glass slide with the Vectashield drop. Again, care was taken to avoid air bubbles. Once the cover glass was in place, the edges were sealed with nail polish, and the sections were ready for the microscope.

3.1.5 Microscopy

A Zeiss LSM510 confocal microscope (Jena, Germany) was used to image the sections. Nile red was excited using the 543-nm He/Ne laser line. FITC-lectin was excited using the 488-nm Ar laser line. Tile scan images were taken using a 20x/0.5 objective. To obtain tile scans, the sections were imaged from periphery to periphery through the center of the tumor using the tile scan function of the microscope. Each single image had a resolution of $512{\times}512$ pixels, and the number of images in the tile scan depended on the size of the tumor section. For tumors

where the tumor diameter through the center exceeded the maximum size of a tile scan, tile scans were taken closer to the periphery where the diameter was smaller. Single images were taken using a 63x/1.4 oil objective. All images were aquired using the same microscopy settings, to allow for quantitative analysis. All images, both tile scans and single images, were taken in channel mode and in lambda mode. A mercury lamp was used when looking through the oculars during positioning before images were taken.

3.2   Analysis

The microscope images were analyzed using the Zeiss LSM510 software.

3.2.1   Quantitative Analysis

Channel mode and lambda mode images were taken to allow for linear unmixing to separate autofluorescence from nile red fluorescence. The Zeiss LSM510 software was used to perform linear unmixing on the lambda mode images. The spectra used for unmixing are shown in Figure 10.

(a) Free nile red   (b) Nile red bound to fat   (c) Autofluorescence
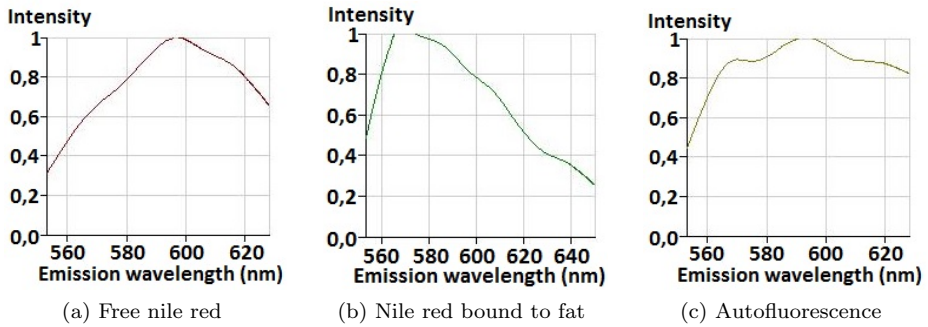
Figure 10: Spectra used for linear unmixing (20x/0.5 objective).

Following unmixing, a matlab routine was run on the images to quantitatively analyze the fluorescence throughout the tile scans. The routine divides the tile scan into segments of a chosen size, and counts the number of pixels with fluorescence intensity higher than a pre-chosen threshold value. The threshold value was set to 0.22. A result file was produced containing the calculated fluorescent area in each segment, and the mean fluorescence of the segment. From this, the total fluorescence of each segment was calculated using of the formula

$$TotFl = MeanInt \times Area, \hspace{3cm} (2)$$

where TotFl is the total fluorescence of each segment, MeanInt is the mean fluorescence of the segment, and Area is the calculated fluorescent area of the segment. The estimated total fluorescence from one section was calculated by adding the total fluorescence from all segments of that section. The average total fluorescence of all five section from each mouse, and the standard deviation, was calculated and plotted for each treatment group. In addition, the average total fluorescence from all mice within each treatment group, and the standard deviation, was calculated and plotted.

The matlab routine was also used to obtain line plots of fluorescence versus relative position in the tile scan. Each tumor section was divided into 10 segments, and the total fluorescence was calculated for each of these 10 segments. In this way, 10 measurement points were obtained. For each measurement point, the average total fluorescence of that relative position was found for each mouse. From this again, the average for each treatment group was found.The average total fluorescence from each segment was plotted against relative position from 0-1 as a line plot. Five different figures were produced: One for each of the four treatment groups, each containing one graph per mouse, and one for all treatments combined, containing one graph per treatment group. To produce the plots, the average of the total fluorescence in each segment (position) of all sections from one mouse was found. For the plot comparing treatment groups, the average of the total fluorescence in each position from all of the mice was found.

3.2.2 Qualitative Analysis

The aim of the qualititative analysis was to investigate whether there was a qualitative difference in the nile red or nanoparticle distribution in the tumor between the different treatment groups. To do this, images from the different treatment groups and from different mice within the same treatment group were compared.

In some cases the brightness and contrast of the image were adjusted, often to enhance the background of the image. When the purpose of a figure was to directly compare images, the brightness and contrast were adjusted the same amount for all images in the figure.

The nile red fluorescence wavelength differs depending on the hydrophobicity of the molecules that nile red is bound to [15]. This can also be seen in Figure 10. This property of nile red was used in the qualitative analysis of the images to try to determine what nile red binds to in the tumor tissue.

4 Results

The total fluorescence was calculated for every section, and the average total fluorescence of all sections was found for each mouse. Subsequently, the average total fluorescence of all mice in each treatment group was found, in addition to the standard deviation. These data are presented in Figure 11, which shows the average total fluorescence per tumor. The figure shows how the total fluorescence per tumor varies between different treatment groups. Based on the large standard deviations in Figure 11, there seems to be no difference in fluorescence from mice having received ultrasound treatment and mice not having received ultrasound treatment, and no difference between the three different ultrasound treatment groups.
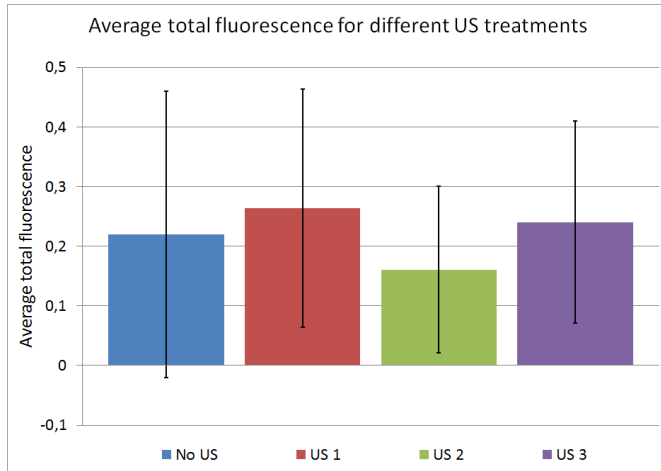
Figure 11: Average total fluorescence per tumor for the different treatment groups. US 1 is 1 MHz and MI = 0.1, US 2 is 1 MHz and MI = 0.4 and US 3 is 1 MHz and MI = 0.4 + 5 MHz and MI = 2.24.

To investigate how the total fluorescence varies between mice within the same treatment group, the average total fluorescence of all sections from each mouse was plotted for mice within the same treatment group. These plots are shown in Figure 12. Each plot in Figure 12 presents data from all mice within one treatment group, and each bar in the plots represents one mouse. The figure thus shows how the total fluorescence per tumor varies between different mice from the same treatment group. Due to the large standard deviations there seems to be no difference between different mice receiving the same treatment. However, when Figure 12 is compared to Figure 11 it becomes evident that the variations between mice within the same treatment groups is even larger than the variation between

the different treatment groups. Even the variations between different sections from the same mouse must be very large, judging from the standard deviations in Figure 12.
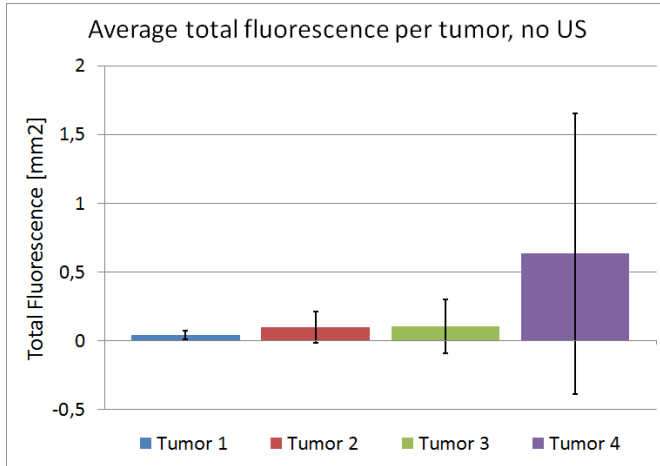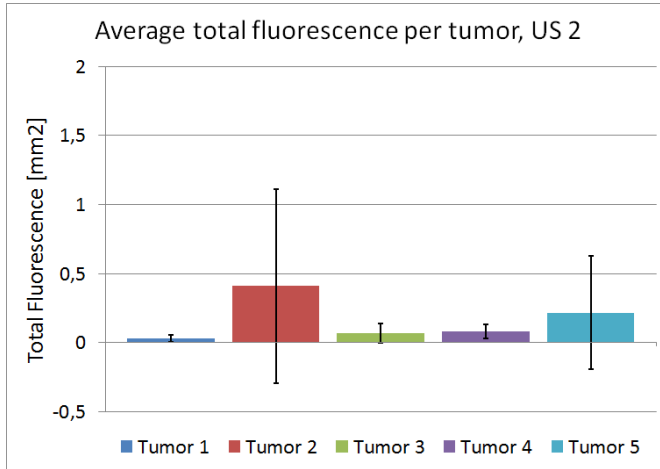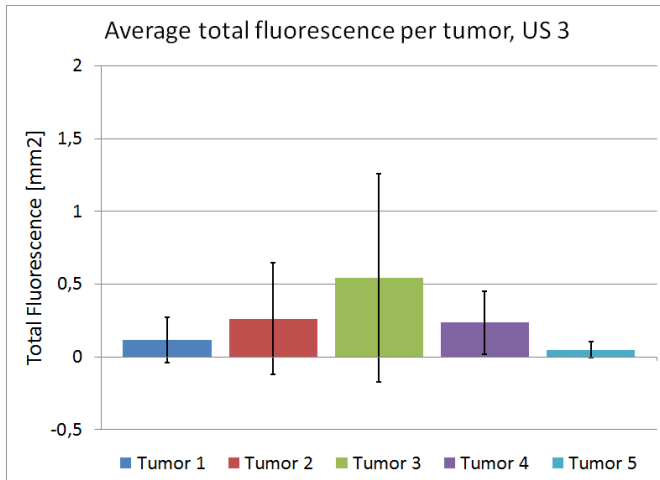

(a) No US.
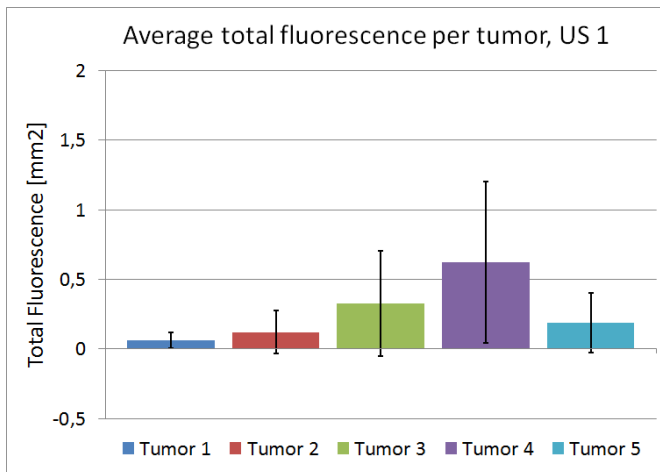
(b) 1 MHz and MI = 0.1 (US 1).

Figure 12: Average total fluorescence per tumor for mice within same treatment group. Each plot represents one treatment group and each bar in the plots represents one mouse. (a) shows average total fluorescence for mice having received no US treatment, and (b) for mice having received US 1.

(c) 1 MHz and MI = 0.4 (US 2).

(d) 1 MHz and MI = 0.4 + 5 MHz and MI = 2.24 (US 3).

Figure 12: Average total fluorescence per tumor for mice within same treatment group. Each plot represents one treatment group and each bar in the plots represents one mouse. (c) shows average total fluorescence for mice having received US 2, and (d) for mice having received US 3.

Before quantitative analysis could be performed on the tile scans, they had to be linearly unmixed. For some of the tile scans, linear unmixing resulted in an image where a "nile red tint" was suddenly introduced that was not present in the original image. Examples of this are shown in Figure 13. Here, green represents nile red

bound to fat. From Figure 13 it is obvious that this unmixing error occured to varying degrees in the different sections. Most sections came out slightly greener than the original, some images came out intensely green across the entire tile scan, while in some sections no false nile red was introduced. This introduction of false nile red in some sections affected further quantitative analysis. As a threshold is chosen in the matlab routine above which a pixel is counted as fluorescent, more pixels were counted as fluorescent in the images where a green tint had been introduced. When it was obvious that the unmixing was erroneous, that section was excluded from further analysis.

(a) A lot of false nile red fluorescence has been introduced in the unmixed image. Section is excluded from further analysis.
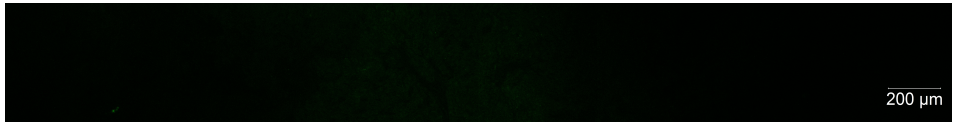
(b) Some false nile red fluorescence has been introduced in the unmixed image. Section might be excluded from further analysis.
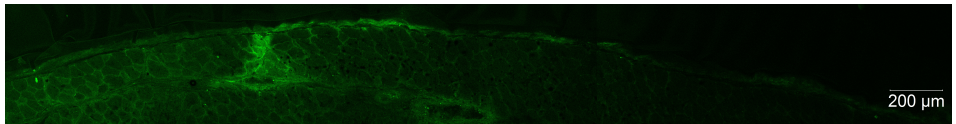
(b) No false nile red fluorescence has been introduced in the unmixed image; however, some nile red fluorescence from the original image has been interpreted as not being nile red bound to fat. Section is included in further analysis. This tile scan is from the periphery of the tumor and most likely shows normal tissue instead of tumor tissue.

Figure 13: Confocal tile scans from three different sections, before (top images) and after (bottom images) unmixing. In the original images, green represents nile red fluorescence, while in the unmixed images green represents nile red bound to fat.

To investigate how the nile red fluorescence varies with relative position in the tumor, line plots of total fluorescence versus relative position in the tile scan were

made. Figure 14 shows the line plots comparing treatment groups. In this figure, each graph represents one treatment group. Comparing the four graphs in Figure 14, there seems to be no real difference between the different treatment groups. The fluorescence is generally quite low; however, there seems to be a trend indicating that the fluorescence intensity is higher in the periphery of the tumors and in some areas further into the tumor. However, the standard deviation is very high (see Appendix), and hence it cannot be concluded that the fluorescence really is higher in some areas of the tumor.
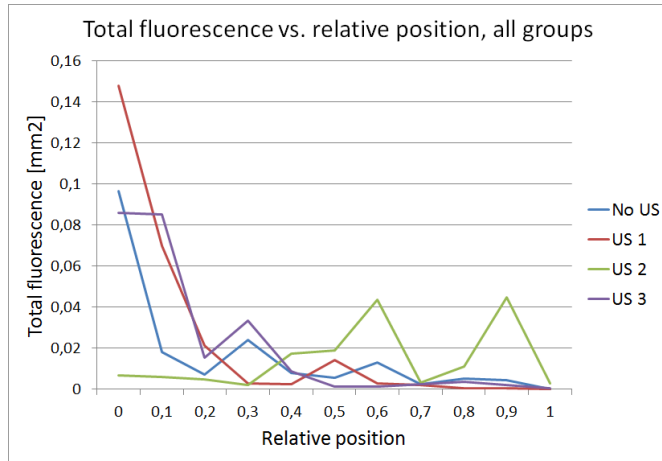
Figure 14: Line plots showing average total fluorescence intensity versus relative position in the tile scan. Each graph represents one treatment group. US 1 is 1 MHz and MI = 0.1, US 2 is 1 MHz and MI = 0.4, and US 3 is 1 MHz and MI = 0.4 + 5 MHz and MI = 2.24. There seems to be no real difference between the treatment group, except for indications of higher fluorescence in the periphery of the tumors and in some areas further into the tumor.

Line plots were also made comparing the fluorescence at different positions in the tumor for the different mice within the same treatment group. These plots are shown in Figure 15. Figure 15 basically shows the same as Figure 14. In general, there is not much fluorescence, but there seems to be higher fluorescence in the periphery of the tumors. There also seems to be higher fluorescence in some areas further into the tumor sections. Figure 15c stands out as the fluorescence does not seem to be higher in the periphery, only at certain locations toward the center of the tumors. The standard deviation is again very high (see Appendix), and as before it cannot be concluded that the fluorescence is higher in some areas.
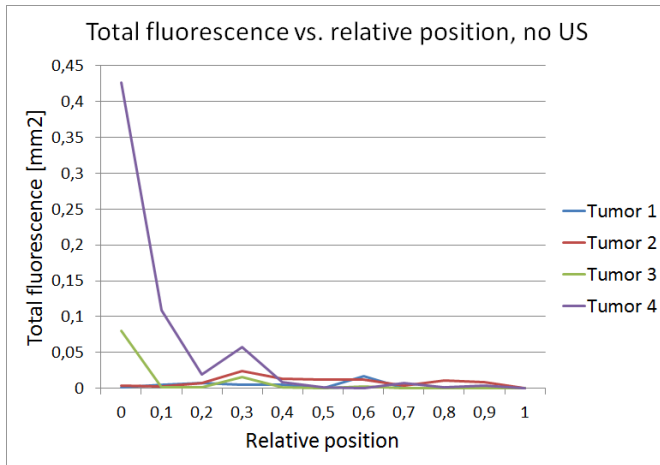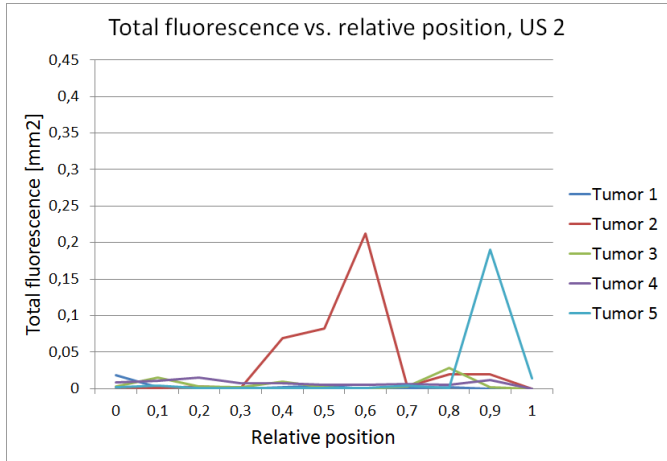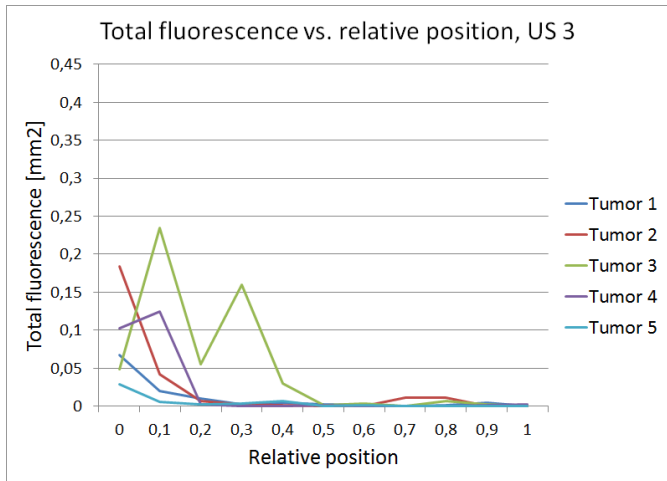
(a) No US.
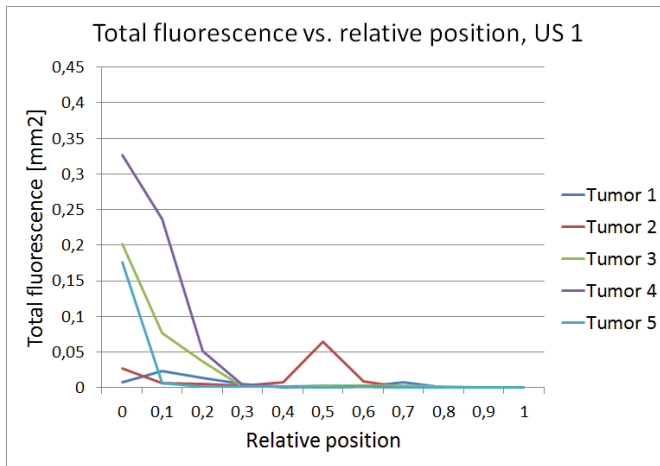
(b) 1 MHz and MI = 0.1 (US 1).

Figure 15: Line plots showing average total fluorescence intensity versus relative position in the tile scan. Each graph represents one mouse. (a) shows the average total fluorescence for mice having received no ultrasound treatment, and (b) for mice having received US 1.

(c) 1 MHz and MI = 0.4 (US 2).

(d) 1 MHz and MI = 0.4 + 5 MHz and MI = 2.24 (US 3).

Figure 15: Line plots showing average total fluorescence intensity versus relative position in the tile scan. Each graph represents one mouse. (c) shows the average total fluorescence for mice having received US 2, and (d) for mice having received US 3.

A selection of confocal images are shown in Figures 16, 17, 18 and 19. Each figure contains six selected images from mice within one treatment group; three from the periphery of the sections and three from the center of the sections. The images selected are a representative collection from the tumors in each treatment group.

The purpose is to qualitatively compare how the nile red distribution is in tumors from different treatment groups. Figure 16 shows images from mice having received no ultrasound treatment, and Figures 17, 18 and 19 show images from mice having received US 1, 2 and 3, respectively. Brightness and contrast have been adjusted in some of the images. It is evident from the images that the larger green spots, or "clouds", that are seen e.g. in Figures 16e, 17e, 18d and 19d are mainly seen in the periphery of the tumors, although in some cases they can also be observed in the center of the tumor. When comparing the different treatments, the green clouds are more intense in the mice that have received ultrasound treatment compared to the mice that have not received ultrasound treatment. The images from the mouse that received no nanoparticles and no ultrasound treatment did not contain any of these clouds. In addition, it seems that the fluorescence in the center of the tumors is more localized to small, intense, green spots in the mice that received no ultrasound treatment, whereas the nile red fluorescence seems to be more evenly distributed in the mice that did receive ultrasound treatment. Some of the images from the tumor periphery most likely show normal tissue instead of tumor tissue.
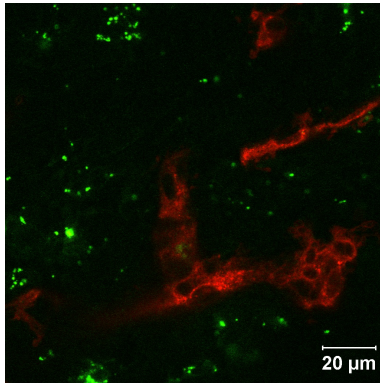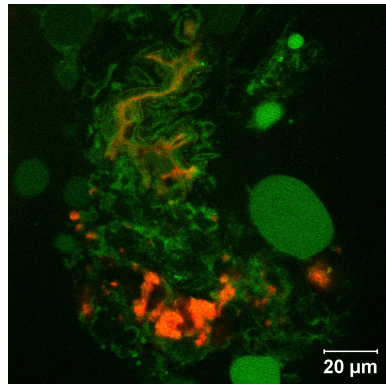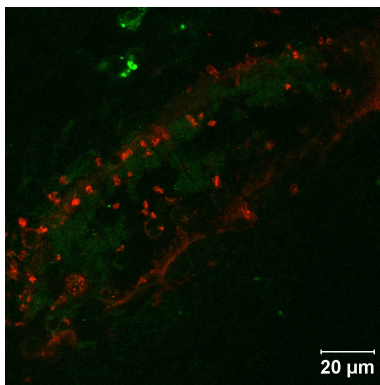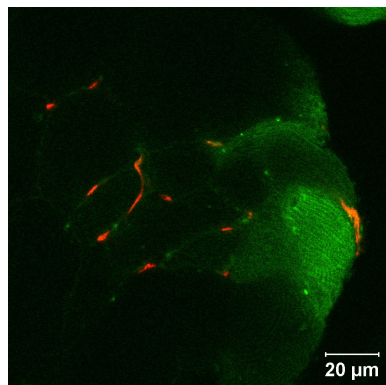
(a) Center.
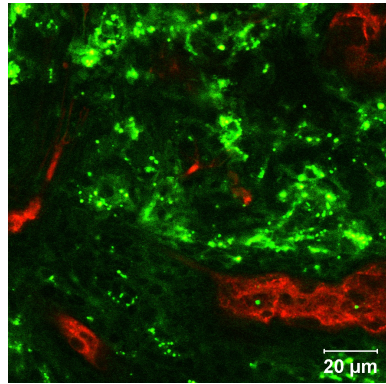
(d) Periphery.
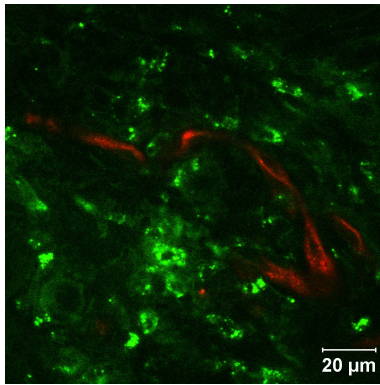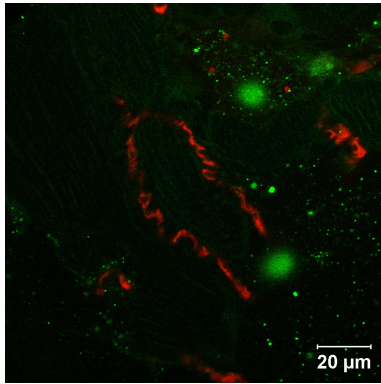

(b) Center.
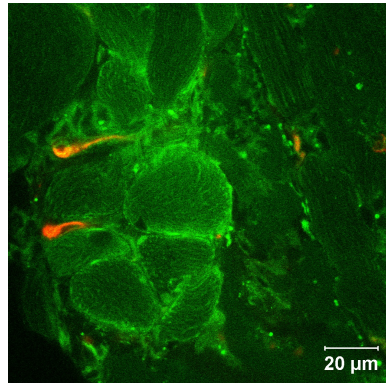

(e) Periphery.

(c) Center.

(f) Periphery.

Figure 16: A selection of confocal images from mice having received no ultrasound treatment.

(a) Center.

(d) Periphery.

(b) Center.

(e) Periphery.

(c) Center.

(f) Periphery.

Figure 17: A selection of confocal images from mice having received US 1 (1 MHz and MI = 0.1).

(a) Center.

(d) Periphery.

(b) Center.

(e) Periphery.
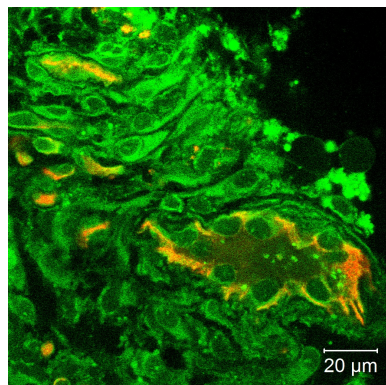
(c) Center.

(f) Periphery.

Figure 18: A selection of confocal images from mice having received US 2 (1 MHz and MI = 0.4).
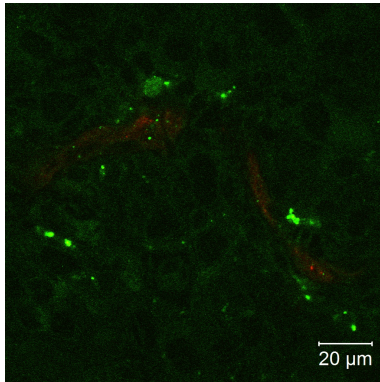
(a) Center.
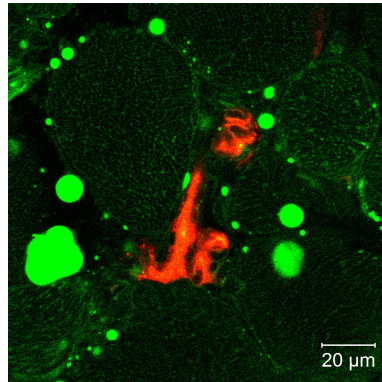
(d) Periphery.
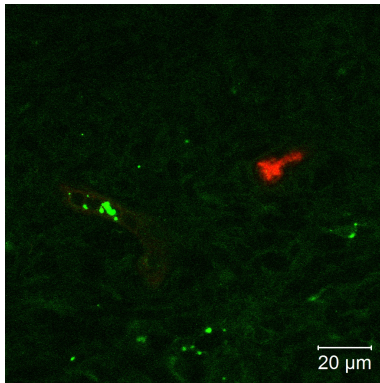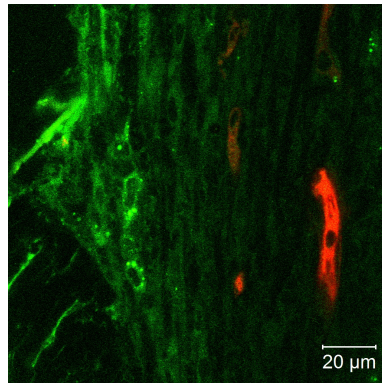
(b) Center.
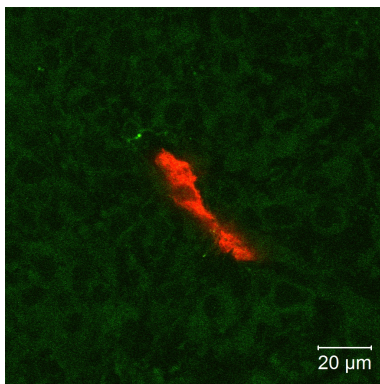
(e) Periphery.

(c) Center.
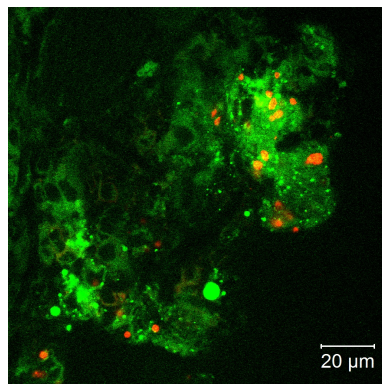
(f) Periphery.
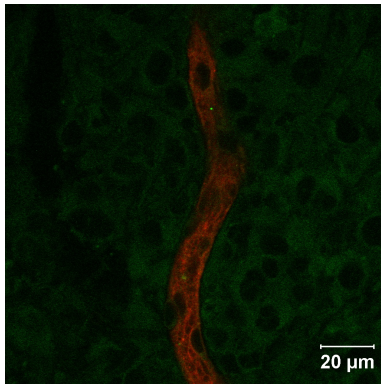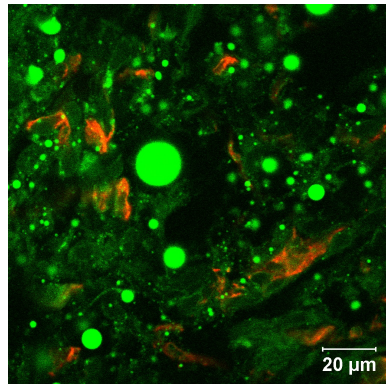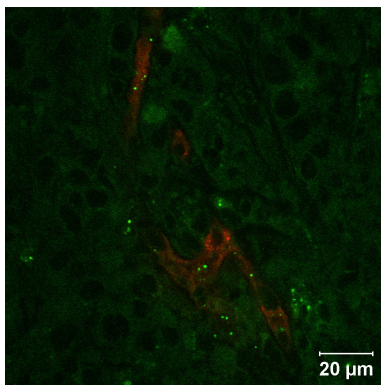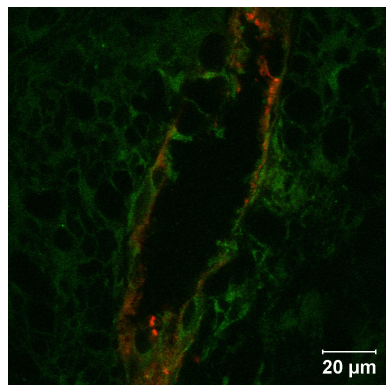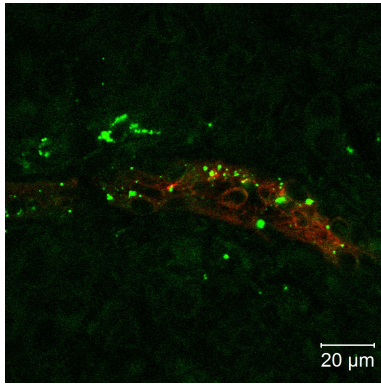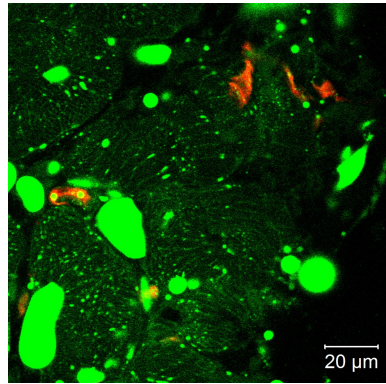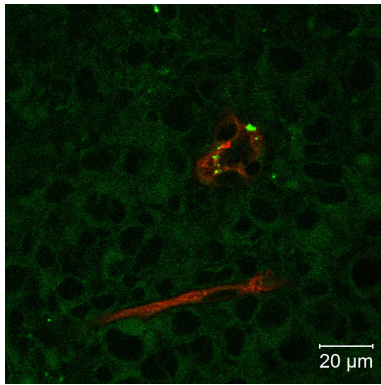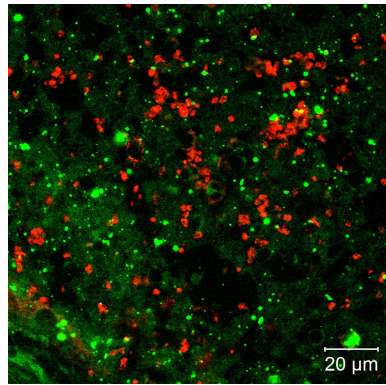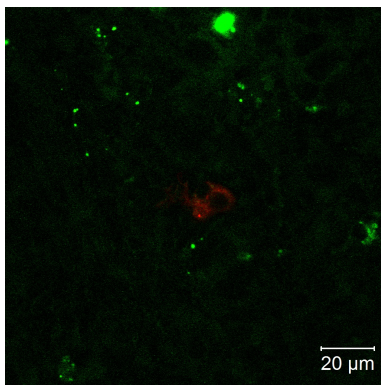
Figure 19: A selection of confocal images from mice having received US 3 (1 MHz and MI = 0.4 + 5 MHz and MI = 2.24).

In some of the images in Figures 16, 17, 18 and 19, green fluorescence in a pattern that looks like cells can be seen in the background. In Figure 20 a selection of such images are presented. One central image from each treatment group is included in the figure. In addition, two images from the mouse that received no nanoparticles and no ultrasound are included in the figure; one image from the periphery and one from the center of the tumor. The scale bars in the images show that the background structures are all about 10 μm, a reasonable size for presumed cells. The brightness and contrast have been adjusted by the same amount in all of these images to enhance the cell pattern in the background. As previously mentioned, the nile red seems to be more evenly distributed in the mice that have received ultrasound treatment. The same cell-like background pattern arises in the images from the mouse without nanoparticles, indicating that this pattern could be caused by autofluorescence rather than nile red uptake in cells. The fluorescence in the mouse without nanoparticles is however less intense than in the mice with nanoparticles, so some of the fluorescence in these images might actually be caused by nile red uptake. In the peripheral image of the mouse without nanoparticles, the fluorescence intensity is a lot stronger. However, this image most likely shows normal tissue instead of tumor tissue.
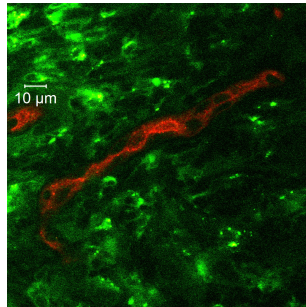
(a) Central section from treatment group without US.
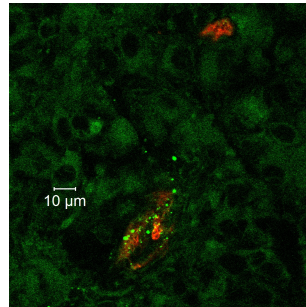
(b) Central section from mouse receiving US 1 (1 MHz and MI = 0.1).
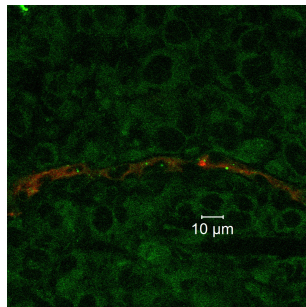
(c) Central section from mouse receiving US 2 (1 MHz and MI = 0.4).
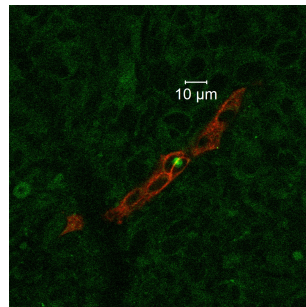
(d) Central section from mouse receiving US 3 (1 MHz and MI = 0.4 + 5 MHz and MI = 2.24).
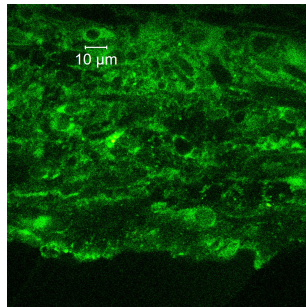
(e) Peripheral section from mouse receiving no nanoparticles and no US treatment. Most likely normal tissue.
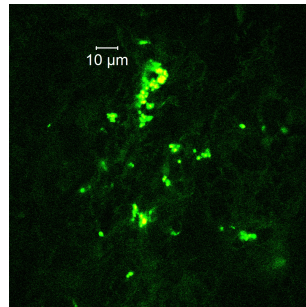
(f) Central section from mouse receiving no nanoparticles and no US treatment.

Figure 20: Selected central images from mice from all treatment groups, showing background with cell-like pattern, and peripheral and central image from mouse without nanoparticles and without ultrasound. Brightness and contrast have been adjusted by the same amount in all images.

As seen in Figure 20 some bright spots are seen in the central image from the mouse without nanoparticles. These bright spots are reminiscent of the bright spots seen in Figure 20a. The small, intense, green spots that are seen in some of the images from mice having received no ultrasound, such as Figure 20a, are thought to be relatively intact nanoparticles. However, it is impossible that the bright, green spots in Figure 20f are nanoparticles, as no nanoparticles were administered to the mouse. In hope to understand more about what the different structures that are seen in the images are, the spectra were extracted from the lambda mode images. These spectra are shown in Figures 21, 22 and 24.
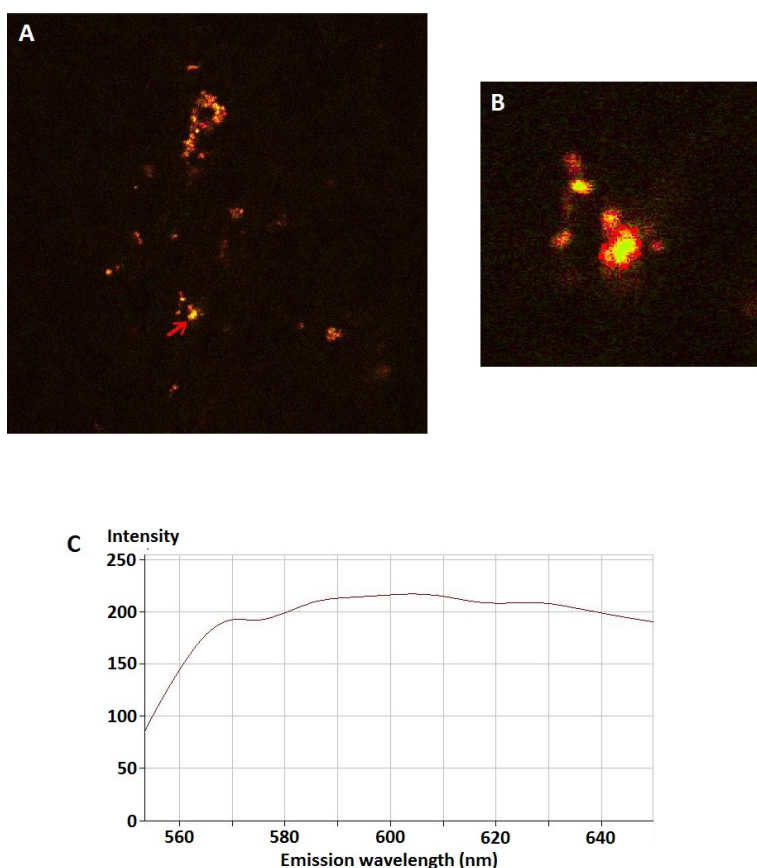
Figure 21: Spectrum from control mouse without administration of nanoparticles and without ultrasound. (A) shows lambda mode image, with an arrow pointing to the structure from which the spectrum was taken. (B) shows a close-up image of the structure, with an outline of where the spectrum was taken. (C) shows the spectrum. There is a maximum at around 605 nm, close to the emission wavelength of the nanoparticles.
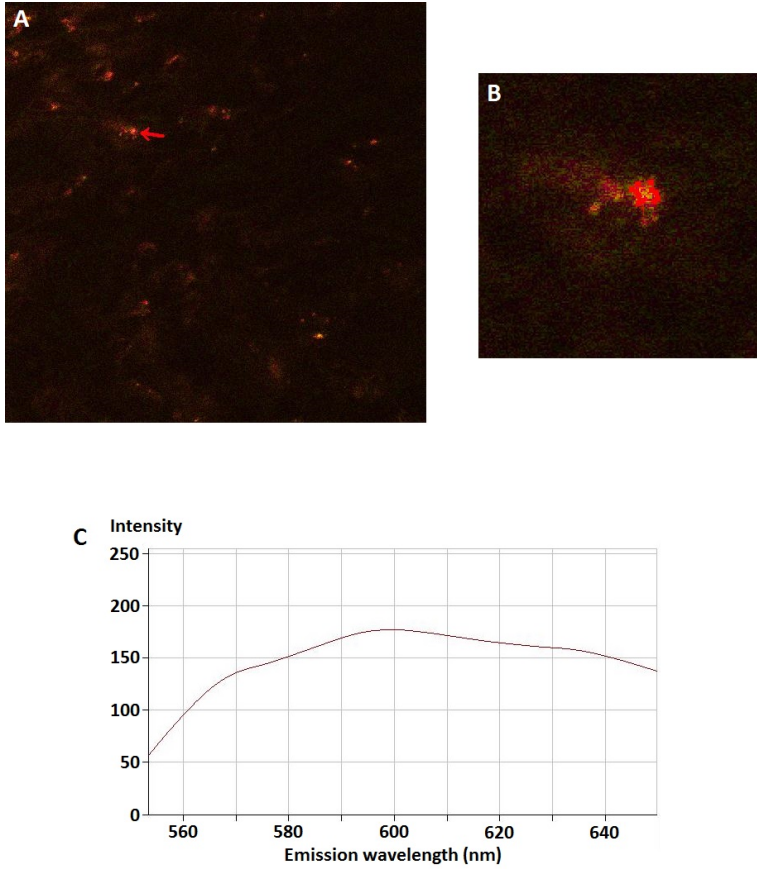
Figure 22: Spectrum from mouse having received nanoparticles, but no ultrasound treatment. (A) shows lambda mode image, with an arrow pointing to the structure from which the spectrum was taken. (B) shows a close-up image of the structure, with an outline of where the spectrum was taken. (C) shows the spectrum. There is a maximum at around 600 nm, close to the emission wavelength of the nanoparticles. However, the maximum from the mouse without nanoparticles lies too close to this maximum, hence it cannot be concluded that the structure is intact nanoparticles.

Figure 21 shows the spectrum of a structure from the mouse that received no nanoparticles. The channel mode image is shown in Figure 20f. The maximum of the spectrum lies at around 605 nm. This is slightly above, but quite close to, the emission wavelength of the nanoparticles (see Figure 10), although it is impossible that this is nanoparticles as no nanoparticles were administered to the mouse. Figure 22 shows the spectrum of a structure that is thought to be intact

nanoparticles. The channel mode image is shown in Figure 20a. The maximum of
the spectrum lies just below 600 nm. This is very close to the emission wavelength
of the nanoparticles, meaning that this structure might in fact be composed of rela-
tively intact nanoparticles. However, since the maxima of the spectra in Figure 21
and Figure 22 lie so close together in wavelength, it is impossible to conclude that
this is in fact nanoparticles and not just an artefact.

Figure 24 shows the spectrum from a green "cloud", and the spectrum from another
structure thought to be intact nanoparticles. The maximum of the spectrum from
the cloud is placed at around 590 nm. The spectra of several different clouds were
taken, and they all had maxima at around 590 nm. This is slightly left-shifted
compared to the spectrum of the nanoparticles. The maximum of the spectrum
from the structure thought to be nanoparticles lies at around 605 nm. This is
slightly right-shifted compared to the nanoparticles, but again the maximum lies
too close to that of the artefacts and henceit can not be concluded that this is
nanoparticles. The channel mode version of the image from Figure 24 is shown in
Figure 23.
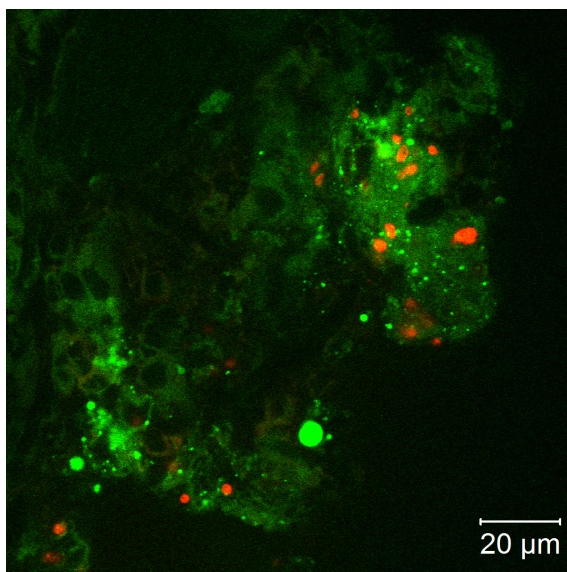
Figure 23: Channel mode version of the image from which the spectra in Figure 24
were taken.
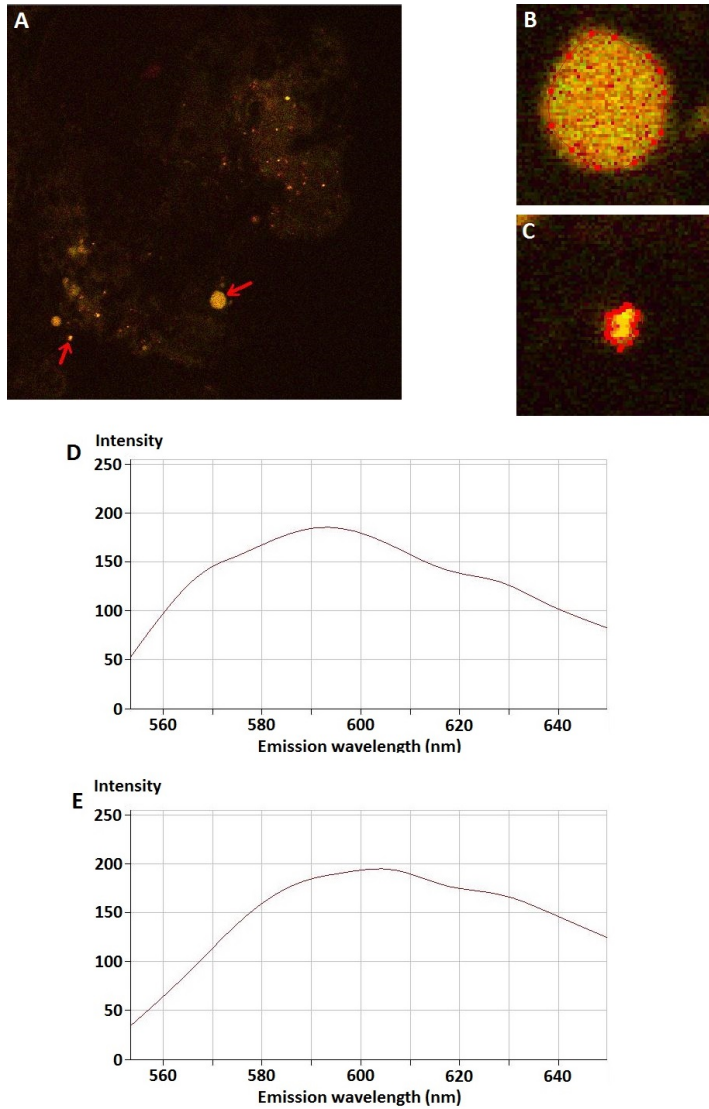
Figure 24: Spectra from mouse having received nanoparticles, and US 3. (A) shows lambda mode image, with an arrow pointing to the structures from which the spectra were taken. (B) and (C) show close-up images of the structures, with outlines of where the spectra were taken. (D) and (E) show the spectra from structures (B) and (C), respectively. For structure (B) there is a maximum at around 590 nm. This is slightly left-shifted compared to the nanoparticles, and might therefore be nile red bound to fat. For structure (C) there is a maximum at around 605 nm. Although this is close to the maximum for the nanoparticles, it is too close to the emission maximum from the mouse having received no nanoparticles, hence it cannot be concluded that this is intact nanoparticles.

5 Discussion

5.1 Methods

Image aquisition During tile scan image aquisition, the aim was to take tile scans from one periphery of the tumor section to the the other periphery, through the center of the tumor. However, as the tile scan function of the microscope software has a maximum allowed number of images per tile scan, it is impossible to take a tile scan through the center of the tumor if the section diameter exceeds this maximum tile scan length. As several sections were too large, the tile scan of these sections had to be taken toward the rim of the tumor, where the diameter was smaller. Hence, several tile scans are instead taken from the topmost or bottommost positions of the sections.

Along the tumor rim some normal tissue can often be seen; a cap of collagen and elastin. Some normal tissue will inevitably be included in the tile scans as long as it is present along the rim of the tumor, and if the tile scan is taken too far toward the edges, a lot of the tile scan will be of normal tissue instead of tumor tissue. It is evident from the images in this study that the cap has a lot of autofluorescence compared to the tumor tissue, and this high fluorescence will affect the analysis. Tile scans taken at or close to the tumor rim will be significantly more fluorescent than tile scans taken through the center of the tumor. The normal tissue is most likely also part of the reason why the fluorescence intensity in the periphery of the tumors seems to be higher in the line plots in Figures 14 and 15.

The statistics of the quantitative analysis would most likely have been significantly improved if all tile scans had been taken through the center of the tumor, and if the normal tissue along the rim of the tumor had not been present, as the standard deviations would have been reduced. Had the standard deviations been smaller, the differences between different treatment groups could possibly have been significant. However, it is also possible that the small differences would completely disappear.

Linear unmixing As previously mentioned, false nile red fluorescence was introduced to several of the tile scans during linear unmixing. This was probably caused by the fact that the recorded reference spectra that were used for linear unmixing were not good enough. If an unreasonable amount of pixels in a tile scan were counted as fluorescent, the tile scan was excluded from further analysis. However, as was seen in Figure 13, this erroneous unmixing occured at varying degrees for different tile scans. It is hard to tell whether some false fluorescence was introduced to all of the sections, or just to a few of them, and deciding which tile scans should be allowed in the analysis and which should not, is challenging. If too many tile scans are excluded, the statistics of the analysis suffer, but if too

many are included, the standard deviations become unreasonably high. This is probably part of the reason why the standard deviations are so high in this study.

Matlab   For the Matlab routine, one single threshold value was chosen for all the sections that were analyzed. This was done to save time, as it would have been extremely time consuming to find a good threshold value separately for each of close to 100 tile scans. However, using a common threshold value for all the sections was not ideal as the autofluorescence level varies between mice, and because of the false nile red fluorescence introduced during linear unmixing. The threshold worked quite well for some sections, but for several of the sections the threshold was either too low, so that pixels were counted that were actually background, or too high, so that not all fluorescent pixels were counted. Adjusting the threshold value might lead to an improvement of the problem. However, a lower threshold value would lead to poorer statistics as more sections would have to be excluded, whereas a higher threshold value would lead to even fewer pixels being counted in the images where too few pixels are counted already. Finding a middle ground that works as well as possible for as many of the tile scans as possible, is challenging.

5.2   Effect of Ultrasound Treatment

Quantitative Analysis   No statistically significant difference is observed between the different treatment groups in the quantitative analysis, due to the very large standard deviations. It is important to stress that although no significant difference is found, this does not necessarily mean that there is no difference between the groups. The standard deviations between mice within the same treatment group, and even between different sections from the same mouse, show that the fluorescence varies just as much, if not more, between sections and between mice as it does between treatment groups. As the large standard deviations are probably due to poor reference spectra for unmixing and normal tissue at the tumor rim, using better spectra and recording better tile scans might give vastly different results.

The plots of average total fluorescence versus relative position in the tumor, presented in Figures 14 and 15, indicate that the fluorescence might be higher at peripheral positions in the tumor. This indication might merely be a result of the normal tissue at the tumor rim being a part of the tile scans. If this is the case, the line plots no longer correctly reflect the distribution of nile red in tumor tissue. The high fluorescence in peripheral positions might also partly be caused by the large, intense, green spots, or "clouds", that are seen in some images, as they are found mainly in the tumor periphery and contribute with a large amount of nile red fluorescence.

In general, the florescence in the tile scans is quite low. This could be due to a too small amount of nile red encapsulated in the nanoparticles, or because nile red is not a well-suited dye for this purpose. Similar nanoparticles have previously been found to be leaking nile red [47]. The overall fluorescence would probably have been higher if the threshold was lower, but that would again mean that more plots would have to be excluded from the analysis.

Qualitative Analysis Although there is no significant quantitative difference between the treatment groups, there are two qualitative differences between the mice that have received ultrasound treatment and the mice that have not. The differences can be observed from the images taken with the 63x/1.4 oil objective.

The first difference is related to the fluorescent "clouds" that are observed in the periphery of the tumors. The clouds are much more intense in the mice that have been treated with ultrasound than in the mice that only have had nanoparticles intravenously administered, but have received no ultrasound treatment. There is no pronounced difference between the clouds in images from mice having received different ultrasound treatments. As the emission spectra of nile red can vary with what nile red is bound to [15]. Nile red spectra are shifted toward shorter wavelengths when the polarity of the solvent decreases [14]; hence, they are shifted toward shorter wavelengths when nile red is bound to a hydrophobic substance. It it seen from Figure 24 that the spectra of these clouds are slightly left-shifted compared to the emission wavelength of the nanoparticles (Figure 10, with a maximum from the clouds at around 590 nm. Hence, it is thought that these clouds might be nile red bound to adipose tissue, which is hydrophobic. Pugliese et al. [43] have shown that ultrasound can lead to alterations in adipocytes and collagen fibers. Thus, the clouds might appear brighter because something happens with the adipose tissue during ultrasound treatment so that more nile red is taken up. It is also possible that the clouds appear brighter because the ultrasound treatment affects the nanoparticles themselves to make them release more nile red, or it could be a combination of both effects. The clouds were not observed in any of the images from the mouse that did not receive nanoparticles. This is an indication that the clouds are indeed caused by free nile red binding to adipose tissue.

The second difference is that the nile red fluorescence in Figure 20, where there appears to be cells in the background, is more diffuse in the mice that have received ultrasound treatment. Some of this diffuse fluorescence could be due to autofluorescence. However, since the background in the mice that have received nanoparticles and ultrasound has a higher fluorescence intensity than that of the mouse without nanoparticles, it could also be partly due to uptake of nile red in cells. It was attempted to obtain an emission spectrum from what was thought to be the inside of the cells. This was challenging, as the spectrum changed at even the slightest relocation of where the spectrum was taken from. This could

be a sign that nile red binds to many different molecules inside the cells and in the tissue, since the nile red spectra vary with the hydrophobicity of the substance that nile red is bound to. As nile red is hydrophobic [15], it would more likely bind to hydrophobic molecules inside the cell than to be free in the cytosol. The fact that the spectrum changes so much could therefore be an indication that nile red is in fact taken up into cells, although it is impossible to draw a conclusion. If nile red is taken up in the cell, it is probably free nile red that has been released from the nanoparticle. Free nile red could be released as a result of the ultrasound treatment, but is could also be released as a result of natural degradement of the nanoparticles in the tumor tissue, or it could be a result of the nanoparticles leaking nile red.

Small, intensely colored, green spots were observed both in the mice that received no ultrasound, and in the mouse that received no nanoparticles and no ultrasound. These spots were thought to be relatively intact nanoparticles. The spectra of the structures were extracted to check this assumption. It turned out that the spectrum maximum of the structure from the mouse that received nanoparticles without ultrasound coincides with the emission wavelength of the nanoparticles at just below 600 nm, meaning that the spots might be intact nanoparticles. However, the maximum also lies close to the maximum of the artefact spectrum from the mouse that received no nanoparticles. The maximum of the emission spectrum for the artefacts might incidentally lie very close to the nanoparticle spectrum, in which case it is still possible that the green spots in the treated mice are in fact nanoparticles, but no certain conclusion can be made. This could also be an indication that the recorded spectra for linear unmixing are not good enough.

6   Conclusions and Further Work

The quantitative analysis resulted in no statistically significant differences between the different treatment groups. The differences between different mice within the same treatment group, and even between different sections from the same mouse, were just as large, if not larger. However, a qualitative difference between the mice that did not receive ultrasound and the mice that did receive ultrasound was found. The mice that received ultrasound had bright, green spots or "clouds" of much higher intensity than the mice that did not receive ultrasound. The mouse that did not receive nanoparticles showed no such clouds. This indicates that the fluorescence from these clouds does come from nile red. Based on the emission spectra, they are thought to be nile red bound to fat. Since the clouds are brighter in mice with ultrasound, nile red must somehow be taken up to a higher degree in fat tissue with ultrasound. Whether this is a result of a change in the fat tissue as a response to the ultrasound or a result of more nile red being released from the nanoparticles as a response to the ultrasound, is not known.

In the future, a different dye than nile red should be used in the nanoparticles, as nile red has been shown to leak out of nanoparticles similar to the ones used in this study. In addition, the nanoparticles used should have a higher fluorescence than the autofluorescence of the mice, so that the autofluorescence is not such a big issue. Better spectra should be taken so that the linear unmixing does not introduce false fluorescence, but rather removes autofluorescence as it is supposed to, and better tile scans should be taken so that they pass through the center of the tumor and do not include such a large amount of normal tissue.

References

[1] S. B. Barnett et al. "Current Status of Research on Biophysical Effects of Ultrasound". In: *Ultrasound in Medicine & Biology* 20 (1994), pp. 205–218.

[2] Wayne M. Becker et al. *The World of the Cell*. 7th ed. Pearson Education, Inc., 2009.

[3] Susannah H. Bloch, Paul A. Dayton, and Katherine W. Ferrara. "Targeted Imaging Using Ultrasound Contrast Agents". In: *Engineering in Medicine and Biology Magazine, IEEE* 23 (2004), pp. 18–29.

[4] Yves Boucher and Rakesh K. Jain. "Microvascular Pressure is the Principal Driving Force for Interstitial Hypertension in Solid Tumors: Implications for Vascular Collapse". In: *Cancer Research* 52 (1992), pp. 5110–5114.

[5] Christopher Earls Brennen. *Cavitation and Bubble Dynamics*. Oxford University Press, 1995.

[6] Iréne Brigger, Catherine Dubernet, and Patrick Couvreur. "Nanoparticles in Cancer Therapy and Diagnostics". In: *Advanced Drug Delivery Reviews* 64 (2012), pp. 24–36.

[7] Peter Carmeliet and Rakesh K. Jain. "Angiogenesis in Cancer and Other Diseases". In: *Nature* 407 (2000), pp. 249–257.

[8] J. Y. Chapelon et al. "In Vivo Effects of High-Intensity Ultrasound on Prostatic Adenocarcinoma Dunning R3327". In: *Cancer Research* 52 (1992), pp. 6353–6357.

[9] Vikash P. Chauhan et al. "Delivery of Molecular and Nanoscale Medicine to Tumors: Transport Barriers and Strategies". In: *Annual Review of Chemical and Biomolecular Engineering* 2 (2011), pp. 281–298.

[10] Kwangjae Cho et al. "Therapeutic Nanoparticles for Drug Delivery in Cancer". In: *Clinical Cancer Research* 14 (2008), pp. 1310–1316.

[11] Mary E. Dickinson and Michael W. Davidson. *Introduction to Spectral Imaging and Linear Unmixing*. June 2013. URL: http://zeiss-campus.magnet.fsu.edu/articles/spectralimaging/introduction.html.

[12] J. M. Escoffre et al. "Irinotecan Delivery by Microbubble-Assisted Ultrasound: *In Vitro* Validation and a Pilot Preclinical Study". In: *Molecular Pharmaceutics* (2013).

[13] Sestina Falcone et al. "Macropinocytosis: Regulated Coordination of Endocytic and Exocytic Membrane Traffic Events". In: *Journal of Cell Science* 119 (2006), pp. 4758–4769.

[14] P. Greenspan and S. D. Fowler. "Spectrofluorometric Studies of the Lipid Probe, Nile Red". In: *Journal of Lipid Research* 26 (1985), pp. 781–789.

[15] Phillip Greenspan, Eugene P. Mayer, and Stanley D. Fowler. "Nile Red: A Selective Fluorescent Stain for Intracellular Lipid Droplets". In: *The Journal of Cell Biology* 100 (1985), pp. 965–973.

[16] J. F. Hainfeld et al. "Gold nanoparticles: A New X-ray Contrast Agent". In: *British Journal of Radiology* 79 (2006), pp. 248–253.

[17] Barbara Haley and Eugene Frenkel. "Nanoparticles for Drug Delivery in Cancer Treatment". In: *Urologic Oncology: Seminars and Original Investigations* 26 (2008), pp. 57–64.

[18] G. H. Harrison, E. K. Balcer-Kubiczek, and H. A. Eddy. "Potentiation of Chemotherapy by Low-level Ultrasound". In: *International Journal of Radiation Biology* 59 (1991), pp. 1453–1466.

[19] Victor F. Humphrey. "Ultrasound and Matter - Physical Interactions". In: *Progress in Biophysics and Molecular Biology* 93 (2007), pp. 195–211.

[20] Arun K. Iyer et al. "Exploiting the Enhanced Permeability and Retention Effect for Tumor Targeting". In: *Drug Discovery Today* 11 (2006), pp. 812–818.

[21] Rakesh K. Jain. "Barriers to Drug Delivery in Solid Tumors". In: *Scientific American* 271 (1994), pp. 58–65.

[22] Rakesh K. Jain. "Normalizing Tumor Vasculature With Anti-Angiogenic Therapy: A New Paradigm for Combination Therapy". In: *Nature Medicine* 7 (2001), pp. 987–989.

[23] Rakesh K. Jain. "Transport of Molecules in the Tumor Interstitium: A Review". In: *Cancer Research* 47 (1987), pp. 3039–3051.

[24] Rakesh K. Jain and Triantafyllos Stylianopoulos. "Delivering Nanomedicine to Solid Tumors". In: *Nature Reviews Clinical Oncology* 7 (2010), pp. 653–664.

[25] Siti M. Janib, Ara S. Moses, and J. Andrew MacKay. "Imaging and Drug Delivery Using Theranostic Nanoparticles". In: *Advanced Drug Delivery Reviews* 62 (11 2010), pp. 1052–1063.

[26] Fabian Kiessling et al. "Ultrasound Microbubbles for Molecular Diagnosis, Therapy, and Theranostics". In: *Journal of Nuclear Medicine* 53 (2012), pp. 345–348.

[27] M. Kinoshita et al. "Noninvasive Localized Delivery of Herceptin to the Mouse Brain by MRI-Guided Focused Ultrasound-Induced Blood-Brain Barrier Disruption". In: *Proceedings of the National Academy of Sciences of the United States of America* 103 (2006), pp. 11719–11723.

[28] A. Lawrie et al. "Microbubble-enhanced Ultrasound for Vascular Gene Delivery". In: *Gene Therapy* 7 (2000), pp. 2023–2027.

[29] H. Maeda et al. "Tumor Vascular Permeability and the EPR Effect in Macromolecular Therapeutics: A Review". In: *Journal of Controlled Release* 65 (2000), pp. 271–284.

[30] Hiroshi Maeda. "The Enhanced Permeability and Retention (EPR) Effect in Tumor Vasculature: The Key Role of Tumor-Selective Macromolecular Drug Targeting". In: *Advanced Enzyme Regulation* 41 (2001), pp. 189–207.

[31] Mazin Magzoub, Songwan Jin, and A. S. Verkman. "Enhanced Macromolecule Diffusion Deep in Tumors After Enzymatic Digestion of Extracellular Matrix Collagen and its Associated Proteoglycan Decorin". In: *The FASEB Journal* 22 (1 2008), pp. 276–284.

[32] Philippe Marmottant and Sascha Hilgenfeldt. "Controlled Vesicle Deformation and Lysis by Single Oscillating Bubbles". In: *Nature* 423 (2003), pp. 153–156.

[33] Y. Matsumura and H. Maeda. "A New Concept for Macromolecular Therapeutics in Cancer Chemotherapy: Mechanism of Tumoritropic Accumulation of Protein and the Antitumor Agens SMANCS". In: *Cancer Research* 46 (12 1986), pp. 6387–6392.

[34] Sushmita Mukherjee, Richik N. Ghosh, and Frederick R. Maxfield. "Endocytosis". In: *Physiological Reviews* 77 (1997), pp. 759–803.

[35] Ka-Yun Ng and Yang Liu. "Therapeutic Ultrasound: Its Application in Drug Delivery". In: *Medicinal Research Reviews* 22 (2 2002), pp. 204–223.

[36] W. L. Nyborg. "Biological Effects of Ultrasound: Development of Safety Guidelines. Part II: General Review". In: *Ultrasound in Medicine & Biology* 27 (2001), pp. 301–333.

[37] W. L. Nyborg. "Ultrasonic Microstreaming and Related Phenomena". In: *British Journal of Cancer* 45 (1982), pp. 156–160.

[38] World Health Organization. *Cancer*. June 2013. URL: http://www.who.int/mediacentre/factsheets/fs297/en/.

[39] Stephen W. Paddock. "Principles and Practices of Laser Scanning Confocal Microscopy". In: *Molecular Biotechnology* 16 (2000), pp. 127–149.

[40] Timothy P. Padera et al. "Cancer Cells Compress Intratumor Vessels". In: *Nature* 427 (2004), p. 695.

[41] Lucas Pelkmans and Ari Helenius. "Endocytosis Via Caveolae". In: *Traffic* 3 (2002), pp. 311–320.

[42] William G. Pitt, Ghaleb A. Husseini, and Bryant J. Staples. "Ultrasonic Drug Delivery - a General Review". In: *Expert Opinion Drug Delivery* 1 (2004), pp. 37–56.

[43] D. Pugliese, E. Maiorano, and M. Pascone. "Histopathological Features of Tissue Alterations Induced by low Frequency Ultrasound With Cavitational Effects on Human Adipose Tissue". In: *International Journal of Immunopathology and Pharmacology* 26 (2013), pp. 541–547.

[44] Natalya Rapoport, Zhonggao Gao, and Anne Kennedy. "Multifunctional Nanoparticles for Combining Ultrasonic Tumor Imaging and Targeted Chemotherapy". In: *Journal of the National Cancer Institute* 99 (2007), pp. 1095–1106.

[45] James A. Rooney. "Hemolysis Near an Ultrasonically Pulsating Gas Bubble". In: *Science* 169 (1970), pp. 869–871.

[46] Marit Sletmoen, Catharina de Lange Davies, and Bjørn T. Stokke. *Biophysical Nanotechnologies*. Dept. of Physics, NTNU, 2011.

[47] Kishia Stojcevska Søvik. "Uptake of PEGylated and RGD functionalized nanoparticles in Human Umbilical Vein Endothelial Cells". Project report by Kishia S. Søvik. 2012.

[48] M. Todorova et al. "Antitumor Effects of Combining Metronomic Chemotherapy With the Antivascular Action of Ultrasound Stimulated Microbubbles". In: *International Journal of Cancer* 132 (2013), pp. 2956–2966.

[49] Evan C. Unger et al. "Therapeutic Applications of Microbubbles". In: *European Journal of Radiology* 42 (2 2002), pp. 160–168.

[50] Ibrahim Yildiz, Sourabh Shukla, and Nicole F. Steinmetz. "Applications of Viral Nanoparticles in Medicine". In: *Current Opinion in Biotechnology* 22 (2011), pp. 901–908.

[51] L. Zhang et al. "Nanoparticles in Medicine: Therapeutic Applications and Developments". In: *Clinical Pharmacology & Therapeutics* 83 (2008), pp. 761–769.

Appendix

Tables show data that were used to produce line plots of total fluorescence versus relative position. The standard deviations are very large.

No US

Rel.pos	Tumor 1		Tumor 2		Tumor 3	
	Avg	Std dev	Avg	Std dev	Avg	Std dev
0	0,00097564	0,00125773	0,00333576	0,00252866	0,08067278	0,1605788
0,1	0,00481212	0,00588117	0,00257907	0,00213353	0,00165562	0,00204076
0,2	0,00740963	0,00525898	0,00756054	0,00692413	0,00193646	0,00308815
0,3	0,0048731	0,00509779	0,0241806	0,02946382	0,01589253	0,0309943
0,4	0,00553213	0,01023106	0,01313981	0,01705979	0,0008807	0,00135178
0,5	0,0008242	0,00161539	0,0122059	0,01938157	0,00076966	0,00102302
0,6	0,0167148	0,03213732	0,0124993	0,02129535	0,00304594	0,00566057
0,7	3,2869E-05	6,5739E-05	0,00347446	0,00538961	0,00043035	0,00051799
0,8	0	0	0,01139346	0,02278692	0,00016245	0,00020629
0,9	0	0	0,00908466	0,01739069	0,00019057	0,00038114
1	0	0	0	0	0	0

Rel.pos	Tumor 4		All	
	Avg	Std dev	Avg	Std dev
0	0,42586072	0,70249972	0,04155823	0,06048579
0,1	0,10881337	0,18450775	0,00318371	0,00158313
0,2	0,01893353	0,02386221	0,00536298	0,00217493
0,3	0,05717777	0,09819562	0,01841702	0,01065091
0,4	0,00821833	0,01401259	0,00803255	0,00597833
0,5	0,00181742	0,00287526	0,00596996	0,0072539
0,6	0,00028229	0,00025577	0,01522555	0,00976672
0,7	0,00694502	0,0092468	0,00165183	0,00204969
0,8	0,00194972	0,00290208	0,00575819	0,00866202
0,9	0,00382891	0,00320818	0,00450784	0,0066235
1	0	0	0	0

US 1

Rel.pos	Tumor 1		Tumor 2		Tumor 3	
	Avg	Std dev	Avg	Std dev	Avg	Std dev
0	0,00703714	0,00789222	0,02719316	0,04230343	0,20215414	0,37153946
0,1	0,02341187	0,03620706	0,00590981	0,00412739	0,07699148	0,14886601
0,2	0,01359574	0,02211894	0,00465545	0,0081022	0,03604858	0,05503856
0,3	0,00533797	0,00678257	0,00217163	0,00136049	0,00178831	0,00271688
0,4	0,00047049	0,000584	0,00752376	0,01110977	0,0019533	0,0021338
0,5	0,00289832	0,00454383	0,06483638	0,12746594	0,00215382	0,00370784
0,6	0,00085311	0,00129021	0,00826034	0,01629538	0,00261128	0,00317701
0,7	0,00712652	0,01211656	0,00018246	0,00027112	0,00260791	0,00299597
0,8	0,00051278	0,00088816	0	0	0,00133809	0,00162369
0,9	0	0	0	0	0,00071995	0,0013279
1	0	0	0	0	0	0

Rel.pos	Tumor 4		Tumor 5		All	
	Avg	Std dev	Avg	Std dev	Avg	Std dev
0	0,32716181	0,36721282	0,176373	0,21222229	0,14798385	0,11857611
0,1	0,23626049	0,37003295	0,00670773	0,00659878	0,06985628	0,08714958
0,2	0,05105786	0,09441247	0,00103755	0,00087684	0,02127904	0,01923545
0,3	0,00351056	0,00365508	0,00096926	0,00149955	0,00275555	0,00153012
0,4	0,00102901	0,00080069	0,00115678	0,00231355	0,00242667	0,00259219
0,5	0,00016967	0,00014515	9,15E-05	0,000183	0,01402994	0,0254269
0,6	0,00198661	0,00202244	0,00086713	0,00116704	0,00291569	0,00275579
0,7	4,9515E-05	9,903E-05	0	0	0,00199328	0,00274803
0,8	0,0001005	0,000201	2,638E-05	5,276E-05	0,00039555	0,00050634
0,9	0,00063949	0,0012214	0,00041757	0,00083513	0,0003554	0,00030662
1	0	0	9,5788E-06	1,9158E-05	1,9158E-06	3,8315E-06

US 2

Rel.pos	Tumor 1		Tumor 2		Tumor 3	
	Avg	Std dev	Avg	Std dev	Avg	Std dev
0	0,01794383	0,03074924	0,00172036	0,00155638	0,00331763	0,00150464
0,1	0,00135975	0,0007768	0,00039918	0,00067247	0,01454227	0,02697772
0,2	0,00135353	0,00078017	0,00250952	0,00425922	0,00301565	0,00371904
0,3	0,00018404	0,00012899	0,00096512	0,00167163	0,00167995	0,00201852
0,4	0,0014999	0,0020367	0,06873005	0,11904394	0,00911317	0,01782233
0,5	0,00445305	0,00591749	0,08194799	0,14171385	0,00177669	0,00183292
0,6	0,00017168	0,00018362	0,21238927	0,36767224	0,00012638	0,00022367
0,7	0,00026516	0,00045926	0,00248332	0,00430124	0,00292404	0,00536967
0,8	0,00137661	0,00238436	0,01953853	0,03278563	0,02797541	0,05368048
0,9	4,7459E-05	8,2202E-05	0,01937673	0,03236874	0,00240228	0,00294657
1	0	0	0	0	0	0

Rel.pos	Tumor 4		Tumor 5		All	
	Avg	Std dev	Avg	Std dev	Avg	Std dev
0	0,00892698	0,00935459	0,00163482	0,00227664	0,00670872	0,00621733
0,1	0,01038044	0,01094325	0,00367077	0,0045037	0,00607048	0,00548562
0,2	0,01518811	0,02035244	0,0011488	0,00204721	0,00464312	0,00531845
0,3	0,00747975	0,00926274	0,00054598	0,00066872	0,00217097	0,00270062
0,4	0,00685262	0,00737587	0,00045418	0,00053845	0,01732998	0,02590229
0,5	0,00567727	0,00635817	0,00032537	0,00046913	0,01883608	0,03161268
0,6	0,00481858	0,00641039	0,00032105	0,00056053	0,04356539	0,08443086
0,7	0,00644213	0,00882334	0,00389135	0,00712438	0,0032012	0,0020096
0,8	0,00524902	0,00709378	0,00049268	0,00069637	0,01092645	0,01092823
0,9	0,01194264	0,01691774	0,19017224	0,37960461	0,04478827	0,07301971
1	0	0	0,01345158	0,02690316	0,00269032	0,00538063

US 3

Rel.pos	Tumor 1		Tumor 2		Tumor 3	
	Avg	Std dev	Avg	Std dev	Avg	Std dev
0	0,06692203	0,12809542	0,1839652	0,31429861	0,04846112	0,04864892
0,1	0,02042342	0,02223892	0,04217486	0,06667548	0,2347245	0,33195057
0,2	0,00968146	0,01489253	0,00731334	0,00813098	0,05554664	0,07590985
0,3	0,0021323	0,00249999	0,00219464	0,00167437	0,15959645	0,22536203
0,4	0,00474104	0,0050553	0,00179448	0,00139296	0,02974708	0,03971555
0,5	0,00257456	0,00419043	0,00048868	0,00051772	0,00142316	0,00121855
0,6	0,00164661	0,00164162	0,00044201	0,00061826	0,00312222	0,00249675
0,7	0,00056148	0,00077007	0,0113333	0,01872513	0,00018018	0,00013311
0,8	0,00120433	0,00223398	0,01076799	0,01638102	0,00636267	0,00899817
0,9	0,00503742	0,0085048	0,00068662	0,00069496	0,00287833	0,00407057
1	0	0	7,4254E-05	0,00012861	2,3625E-05	3,341E-05

Rel.pos	Tumor 4		Tumor 5		All	
	Avg	Std dev	Avg	Std dev	Avg	Std dev
0	0,10230146	0,16178067	0,02911531	0,04817889	0,08615302	0,0545377
0,1	0,12402114	0,16105325	0,00553865	0,00771068	0,08537651	0,08515586
0,2	0,00200119	0,00155417	0,00221416	0,00159935	0,01535136	0,0203137
0,3	0,0002594	0,00043668	0,00322771	0,00379295	0,0334821	0,06306444
0,4	0,00061611	0,00104098	0,00667178	0,01015902	0,0087141	0,01073128
0,5	0,00115703	0,00193008	0,00051466	0,00071314	0,00123162	0,00076312
0,6	9,067E-05	0,00013833	0,00109402	0,00189489	0,00127911	0,00106578
0,7	4,2341E-05	6,0503E-05	0,00072448	0,00125483	0,00256836	0,00438944
0,8	0,00022354	0,00037195	3,0514E-05	5,2851E-05	0,00371781	0,00421483
0,9	0,00147548	0,0025556	0	0	0,00201557	0,00178864
1	0,00263415	0,00456248	0	0	0,00054641	0,00104422